Available online at www.sciencedirect.com
ScienceDirect
Geochimica et Cosmochimica Acta 72 (2008) 36–68
Geochimica et Cosmochimica Acta
www.elsevier.com/locate/gca

Chemical weathering of a marine terrace chronosequence, Santa Cruz, California I: Interpreting rates and controls based on soil concentration–depth profiles

Art F. White [a,*], Marjorie S. Schulz [a], Davison V. Vivit [a], Alex E. Blum [b], David A. Stonestrom [a], Suzanne P. Anderson [c]

[a] U.S. Geological Survey, Menlo Park, CA 94025, USA
[b] U.S. Geological Survey, Boulder, CO 80303, USA
[c] University of Colorado, Boulder, CO 80309, USA

Received 17 October 2006; accepted in revised form 17 August 2007; available online 13 November 2007

Abstract

The spatial and temporal changes in element and mineral concentrations in regolith profiles in a chronosequence developed on marine terraces along coastal California are interpreted in terms of chemical weathering rates and processes. In regoliths up to 15 m deep and 226 kyrs old, quartz-normalized mass transfer coefficients indicate non-stoichiometric preferential release of Sr > Ca > Na from plagioclase along with lesser amounts of K, Rb and Ba derived from K-feldspar. Smectite weathering results in the loss of Mg and concurrent incorporation of Al and Fe into secondary kaolinite and Fe-oxides in shallow argillic horizons. Elemental losses from weathering of the Santa Cruz terraces fall within the range of those for other marine terraces along the Pacific Coast of North America.

Residual amounts of plagioclase and K-feldspar decrease with terrace depth and increasing age. The gradient of the weathering profile b_s is defined by the ratio of the weathering rate, R to the velocity at which the profile penetrates into the protolith. A spreadsheet calculator further refines profile geometries, demonstrating that the non-linear regions at low residual feldspar concentrations at shallow depth are dominated by exponential changes in mineral surface-to-volume ratios and at high residual feldspar concentrations, at greater depth, by the approach to thermodynamic saturation. These parameters are of secondary importance to the fluid flux q_h, which in thermodynamically saturated pore water, controls the weathering velocity and mineral losses from the profiles. Long-term fluid fluxes required to reproduce the feldspar weathering profiles are in agreement with contemporary values based on solute Cl balances ($q_h = 0.025$–0.17 m yr^{-1}).

During saturation-controlled and solute-limited weathering, the greater loss of plagioclase relative to K-feldspar is dependent on the large difference in their respective solubilities instead of the small difference between their respective reaction kinetics. The steady-state weathering rate under such conditions is defined as

$$R = \left[q_h \cdot \frac{m_{sol}}{M_{total}}\right] \cdot \left[\frac{1}{S_v \cdot b_s}\right].$$

The product of q_h and the ratio of solubilized to solid state feldspar (m_{sat}/M_{total}) define the weathering velocity. The weathering gradient b_s reflects the kinetic rate of reaction where S_v is the volumetric surface area of the residual feldspar. Both this rate expression and the spreadsheet calculations produce similar plagioclase weathering rates ($R = 5$–14×10^{-16} mol m^{-2} s^{-1}) which agree with those reported for other environments of comparable climate and age. Weathering-dependent concentration

* Corresponding author. Fax: +1 650 329 4538.
E-mail address: afwhite@usgs.gov (A.F. White).

0016-7037/$ - see front matter Published by Elsevier Ltd.
doi:10.1016/j.gca.2007.08.029

profiles are commonly described in literature. The present paper provides methods by which these data can yield a more fundamental understanding of the weathering processes involved.
Published by Elsevier Ltd.

1. INTRODUCTION

Chemical weathering and related hydrologic and biologic processes at the Earth's surface or "critical zone" can be addressed from two perspectives, either on a geologic time scale based on solid state changes in the regolith or on a contemporary time scale based on present day solute compositions and fluxes (White, 2003). Long-term weathering, occurring over tens of thousands to millions of years, reflects the integration of intrinsic changes in mineral properties and abundances, as well as the extrinsic long-term changes in climate, soil permeability and physical erosion. In contrast, contemporary weathering reflects current fluid residence times in soils, effects of seasonal-to-decadal scale changes in precipitation, temperature, and possible anthropogenic influences.

A chronosequence is a set of soils that differ in age of formation but have similar parent material and form under similar climatic, topographic and biological regimes. As such, soil chronosequences are ideal environments in which to simultaneously compare critical zone processes over both geologic and contemporary time scales and to determine if present-day weathering fluxes and rates are comparable to those of the past (White et al., 1996; Blum and Erel, 1997; Stewart et al., 2001; White et al., 2005).

In his landmark work, Jenny (1941) was the first to recognize that the relevance of marine terrace chronosequences extended far beyond the limited geographic confines of the landforms themselves. Data from marine terraces near Mendocino, California helped Jenny to define the primary state factors responsible for soil evolution. Brimhall and Dietrich (1987) used these same chronosequence soils in developing quantitative approaches to volumetric strain and mass transfer associated with chemical weathering. These methods are now widely used in weathering studies, including those involving other marine terraces along the west coast of the United States (Merritts et al., 1992; Langley-Turnbaugh and Bockheim, 1998).

The present paper emphasizes the long term, solid-state aspects of chemical weathering, which include describing elemental distributions and identifying weathering reactions involving major primary and secondary minerals in marine terraces distributed along the coast near Santa Cruz, California. The paper will consider how these components become distributed within vertical profiles taken through individual terraces and how the profiles change as the chronosequence develops. Finally, a discussion is presented as to how the spatial and temporal evolution of these profiles can be used to interpret basic controls on silicate weathering.

The present paper is the first of several being prepared which describe differing aspects of the Santa Cruz terraces. Following papers consider contemporary chemical weathering, including detailed descriptions of solute compositions, atmospheric inputs and hydrologic and biologic processes. Additional efforts are also underway in developing a comprehensive model that will integrate both long term and contemporary aspects of weathering.

2. SITE CHARACTERIZATION

Marine terraces, distributed along the west coast of North America, began as wave cut platforms during high stands of sea level. The physical definition and width of a platform depends on several factors including the duration of the sea-level high stand, the wave intensity, and the bedrock strength (Bradley and Griggs, 1976; Anderson et al., 1999). Sediments deposited on these platforms commonly consist of beach deposits, finer grained near-shore (neritic) sediments and eolian deposits such as sand dunes (Bradley, 1957). Platform formation is accompanied by tectonic uplift which eventually strands the terrace sediments above subsequent marine high stands.

The present study involves a sequence of five marine terraces situated within and northwest of the city of Santa Cruz, California, adjacent to the Pacific Ocean, and approximately 50 km SW of San Francisco (Fig. 1). The study area has a Mediterranean climate with cool wet winters and warm dry summers. The terraces are under the orthographic influence of Ben Lomond Mountain (max elev. = 805 m) with the highest terrace (average elevation = 190 m) receiving about 25% more rainfall than the lowest (average elevation = 6 m). The average annual rainfall for the city of Santa Cruz, California is 727 mm with an average temperature of 13.4 °C.

The nomenclatures used to describe the Santa Cruz terraces are listed in Table 1. For the present study, the terraces will be designated, from youngest to oldest, SCT 1 through SCT 5. The geographic distribution of the terrace surfaces, shown in Fig. 1A, indicates the lateral extent of successively older terraces diminishes with age due principally to head-wall incision by stream channels. The maximum elevation difference between SCT 1 and SCT 5 is about 180 m.

2.1. Geology

Local geology is dominated by Ben Lomond Mountain, a prominent asymmetric dome of Cretaceous crystalline rocks comprised of the Ben Lomond Granite (granodiorite to quartz diorite) and smaller amounts of gabbro that were intruded into meta-sedimentary rocks of Paleozoic and Mesozoic age (Clark, 1981; Kistler and Champion, 2001).

The Miocene Santa Cruz Mudstone and Santa Margarita Sandstone depositionally lap onto this dome complex and comprise the bedrock of the marine terraces (Fig. 1C). The Santa Cruz mudstone ranges from a siliceous, organic-rich mudstone to a porcelanite (Clark,

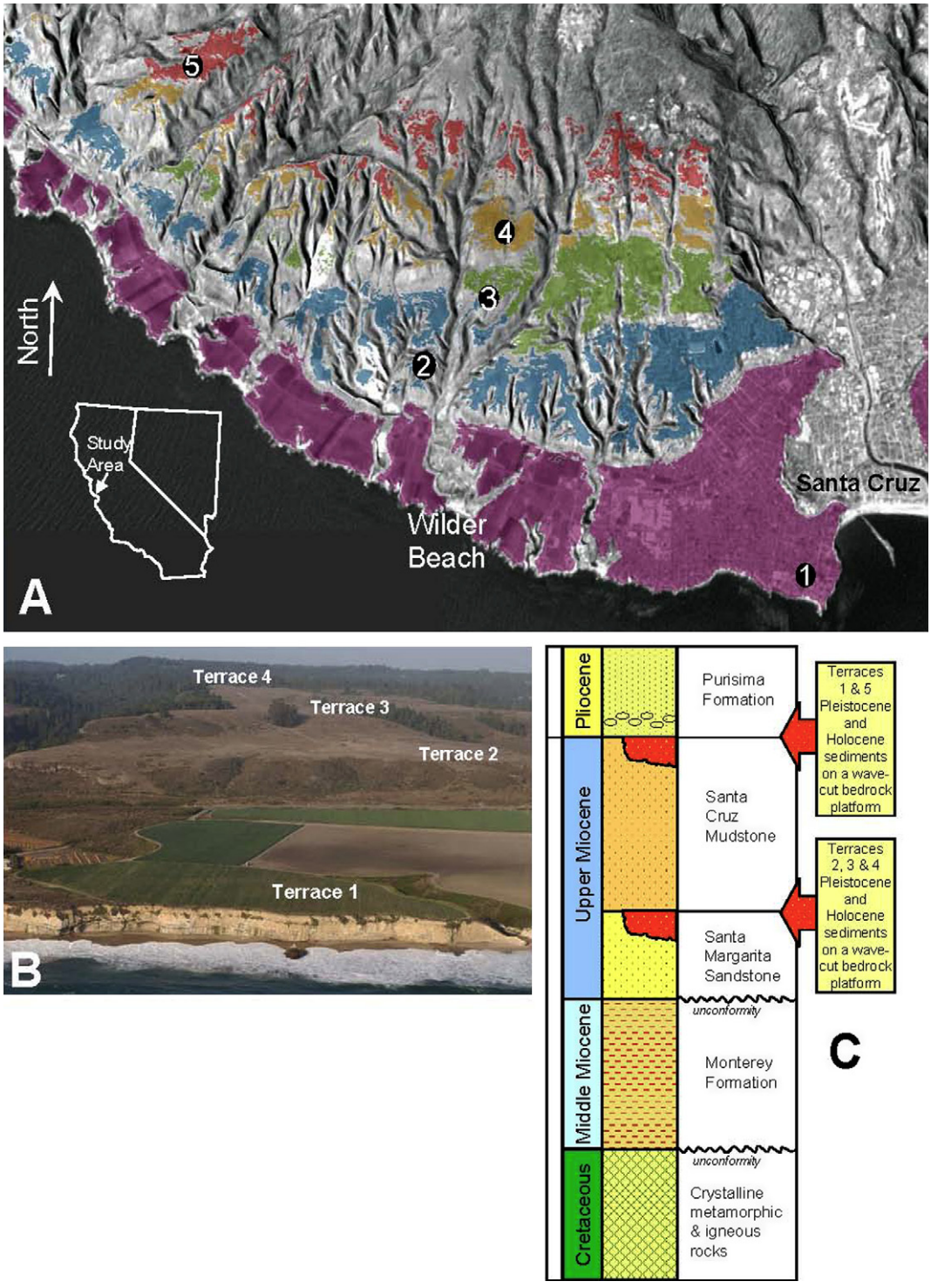

Fig. 1. Spatial distributions of the Santa Cruz terraces. (A) Terrace topographies computationally generated from a U.S. Geological Survey GIS data base and limited to areas with slopes <5%. Numeration refers to sample sites. (B) Aerial view of terraces SCT 1 thru SCT 4 from north of Table Rock. (C) Simplified stratigraphic sequence for Santa Cruz area, including the position of wave-cut platforms.

1981) but contains very little clay (El-Sabbagh and Garrison, 1990). The formation produces relatively wide wave-cut platforms and coherent cliffs that mark both present-day and paleo-seacliffs (Fig. 1B). The Santa Margarita sandstone is clean, well-sorted and poorly-cemented sandstone. Where the sandstone comprises the bedrock of the wave-cut platform, the terraces are deeply incised into the landscape, in some cases obliterating pre-existing terraces.

Regionally, the area is bounded to the northeast by the San Andreas Fault and to the southwest by the San

Table 1
Santa Cruz terrace designations and ages (kyrs)

Terrace designations, this study	Ages utilized in this study	Previous terrace designations		Estimated ages[a]				
				Hanks et al. (1984) (SAGT)	Lajoie et al. (1991) (SAGT)	Weber et al. (1999) (SAGT)	Perg et al. (2001) (CRN)	Muhs et al. (2002) (U-series)
SCT 1	65[c]	Santa Cruz	Davenport platform	83	81	80	65[c]	71–81
	65[c]		Hwy 1 platform	104	124	103	65[c]	nd
	nd	Cement		120	320	125	nd	nd
SCT 2	90	Western		230	430	213	90	nd
SCT 3	137	Wilder		370	800	320	137	nd
SCT 4	194[b]	Blackrock		450	1	430	139	nd
SCT 5	226	Quarry		650	1.3	545	226	nd

[a]Age dating methods: SAGT, shoreline angle graphic technique; CRN, cosmogenic radionuclides, U-series, Uranium series ages of solitary corals; nd, not determined; [b]Interpolated from Perg et al., 2001. [c]Davenport and Hwy 1 not differentiated.

Gregorio Fault, both of which contribute to the continued uplift of the Santa Cruz Mountains. The field area is also transected by smaller local faults that produce topographic juxtaposition of the sedimentary rocks comprising the wave-cut platforms. The SCT 2, 3 and 4 terraces, which are incised into the older Santa Margarita Sandstone, are topographically higher than SCT 1 which is incised into younger Santa Cruz Mudstone (Fig. 1C). The oldest SCT 5 terrace is topographically higher than the SCT 2, 3 and 4 terraces but is also incised into the Santa Cruz Mudstone.

The base of each terrace platform is covered with 1–10 m thick deposits derived principally from long shore marine transport of local riverine sediments produced as erosion products from the Santa Cruz Mountains (Perg et al., 2003). In some localities, these marine sediments were subsequently overlain by fluvial, colluvial and aeolian deposits (Bradley, 1957). Smectite, first identified in terrace deposits in the present study, is compositionally and mineralogically similar to clays in the local Purisima Formation that crops out in present-day marine cliffs and on the seafloor shelf offshore from Santa Cruz (Lerbeko, 1956; Eittreim et al., 2002). This seafloor bedrock provides sediment to the shelf and comprises much of the fine-grained fraction of the terrace deposits.

2.2. Terrace ages

The ages of the Santa Cruz terraces were initially estimated by matching terrace shoreline angle elevation with sea level high stands (SAGT method; Table 1). More recently, the SCT 1 terrace was dated at 71–81 kyrs, based on U series on solitary corals (Muhs et al., 2002). The entire terrace series was age-dated at 65–220 kyrs using ^{10}Be (Perg et al., 2001). The two isotopic ages for SCT 1 are similar while the ^{10}Be age dates for the four older terraces are 2–3 times younger than previous SAGT estimates (Table 1).

The present study utilizes the ^{10}Be terrace ages of Perg et al. (2001). The only exception was the SCT 4 terrace which was found to have an anomalously shallow argillic horizon and a lack of a well developed A horizon, suggesting the anthropogenic removal of up to 30 cm of the soil surface. This removal explains the similarity in Perg's ^{10}Be ages for SCT 3 and SCT 4 (137 vs 139 kyrs, respectively in Table 1) which occurs despite significant elevation differences for the two terraces (110 and 160 m respectively, Appendix I). A revised age of 194 kyrs for SCT 4 was derived by interpolating between elevation differences and the ^{10}Be ages of SCT 3 and SCT 5.

2.3. Sampling and analyses

Initial site surveys, conducted during field observations and by hand augering, indicated significant variations in depths and relative coarseness of the terrace deposits and in the nature of the underlying bedrock. Five sites, one on each terrace, were selected for intensive characterization (locations and elevations listed in Appendix I). The selection criteria included the lack of significant physical erosion deduced from the persistence of flat topographical surfaces, a sufficient lateral distance from the toe and edges of paleosea cliffs and the apparent lack of anthropogenic influences, particularly agriculture on the younger terraces. Evidence of human-induced disturbance of the SCT 4 surface was only deduced later in the study.

The selected sites were hand-augered to maximum depths ranging between 2.7 and 15.3 m (Appendix I). Profile sampling at SCT 1 and SCT 5 sites was restricted to terrace deposits which where underlain by the impermeable Santa Cruz Mudstone. Profiles for the SCT 2, SCT 3 and SCT 4 sites incorporated both terrace deposits and portions of the underlying unconsolidated Santa Margarita Sandstone. Except for SCT 2, maximum sampling depths corresponded to the surfaces of permanent water tables. Above these depths, the soils remained unsaturated except for seasonally perched ground water in the older terraces (late winter to early spring) which was confined to argillic horizons at shallow depths (about 1 m). Significant bioturbation, caused by rooting of the predominant grassland vegetation, as well as burrowing by gophers, were generally limited to $<$1 m.

Each site was extensively instrumented to define chemistry, hydrology, climate and biology using methods previous described by White et al. (1996, 2005). Regolith samples characterized in the present paper were air dried and size separated into $<$2.0 and $>$2.0 mm fractions. The lesser size fraction was analyzed by X-ray fluorescence spectrometry (XRF) for major and selected minor elements. Samples were characterized by scanning electron microscopy

(SEM) and mineral compositions analyzed by electron microprobe. Mineral abundances were determined by the computer program ROCKJOCK (Eberl, 2003) which produces quantitative estimates of mineralogy based on powder X-ray diffraction data (XRD). Grain size distributions were determined using a particle size analyzer based on a laser scattering technique.

3. RESULTS

3.1. Elemental distributions

The vertical distributions of major oxides, trace elements, bulk densities and major minerals are listed in Appendix I. Data are inclusive of the terrace deposits, and for the SCT 2, 3, and 4 profiles, portions of the underlying Santa Margarita Sandstone. Also included in Appendix I are averages for analyses of a profile through the sands on present day Wilder Beach which are being deposited on a wave-cut platform currently being incised into the Santa Cruz Mudstone (Fig. 1A).

Both the terrace deposits and the Wilder Beach sands are significantly enriched in Si and depleted in cations, in particular Mg and Ca, relative to the Ben Lomond Granite (Appendix I). These differences reflect subaerial and marine weathering of the granitic sediments prior to deposition on the terrace platforms. In addition, the deeper terrace sediments are enriched in Al and Fe relative to present day beach sands due to the inclusion of clays (Appendix I). As noted by Bradley (1957), present-day beaches are not good analogues for depositional conditions of the terraces because they do not contain a fine-grained clay fraction indicative of offshore sediments.

Subsequent in situ weathering of the terrace deposits and, where present, the underlying Santa Margarita Sandstone, produces depth-dependent elemental profiles. Changes in these weathering profiles are most apparent in the progressive losses of Na and Ca with decreasing depth (Fig. 2). Similar trends are evident for Sr from Appendix I. In the younger SCT 1 and SCT 2 terraces, these losses are generally confined to the terrace deposits; whereas, in the older SCT 3 and SCT 4 terraces, weathering penetrates to significant depths into the Santa Margarita Sandstone.

Weathering profiles for K (Fig. 2), in addition to Rb and Ba (Appendix I), are much shallower than for Na, Ca and Sr and are confined solely to the terrace deposits. The K, Rb and Ba, profiles change less with regolith age, implying that their mobility during weathering is significantly less than for Na, Ca, and Sr. The K, Rb and Ba profiles are also characterized by distinct concentration reversals above about 1 m depth where their concentrations approach those of the deeper less-weathered parts of the regolith. Weathering profiles for Al and Fe are very different than for the other cations shown in Fig. 2, exhibiting significant concentration increases at shallower depths, particularly in the older terraces.

3.2. Primary mineral distributions

The mineralogy of the Ben Lomond Granite (quartz diorite) is dominated by plagioclase followed by quartz and K-feldspar (Appendix I), whereas in the terraces, quartz predominates over plagioclase and K-feldspar. These mineralogical differences, like the elemental differences, were produced, in part, by weathering prior to deposition on the terraces. The average plagioclase compositions in the deep unweathered terrace sediments (An_{25}–An_{33}), as determined by electron microprobe analyses (Table 2), are compositionally similar to the Ben Lomond Granite (Ross, 1972). The terrace K-feldspars are dominantly microcline.

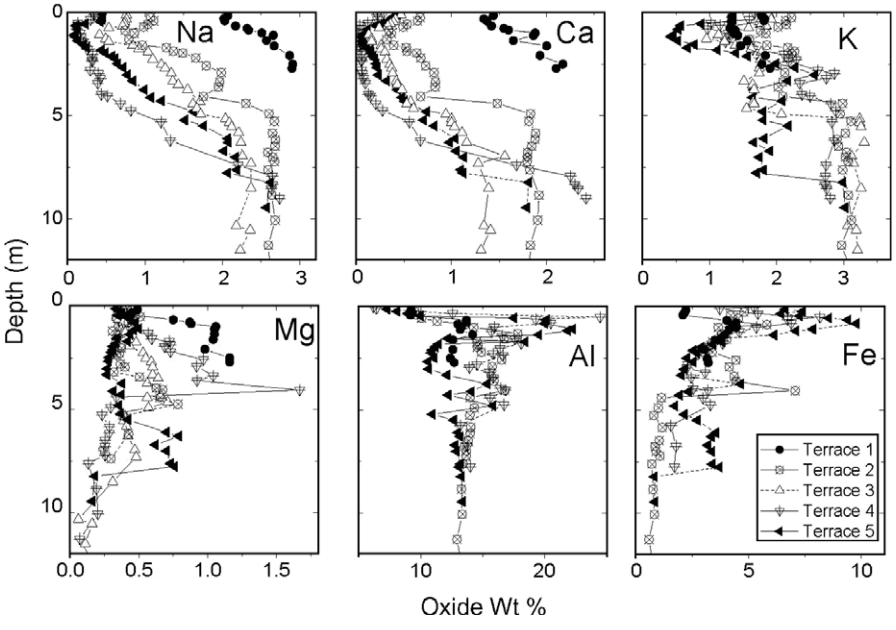

Fig. 2. Selective oxide distributions in Santa Cruz terraces.

Table 2
Chemical compositions and stochiometries of selective minerals in individual terrace profiles (wt%)

	SiO_2	TiO_2	AI_2O_3	FeO[a]	MnO	MgO	CaO	Na_2C	K_2O	SrO	Total	Formula
SCT 1												
Plagioclase	59.7	—	0.2	0.0	—	6.8	7.6	0.2	0.1	0.141	99.6	$Na_{0.66}Ca_{0.33}Al_{1.32}Si_{2.67}O_8$
K-feldspar	64.1	—	18.4	0.1	—	0.0	0.0	1.2	14.8	0.106	98.7	$K_{0.89}Na_{0.11}A_{11.01}Si_{2.99}O_8$
Hornblende	47.8	1.20	6.7	14.6	0.51	13.6	11.7	1.2	0.4	—	97.9	nd
Biotite	35.3	2.69	15.6	19.4	0.30	9.2	0.4	0.1	4.9	—	88.2	nd
SCT 2												
Plagioclase	61.6	—	23.6	0.2	—	0.0	5.2	8.4	0.3	0.151	99.3	$Na_{0.73}Ca_{0.25}Al_{1.24}Si_{2.75}O_8$
K-feldspar	64.0	—	18.4	0.1	—	0.0	0.0	1.0	15.1	0.124	98.8	$K_{0.85}Na_{0.109}A_{10.96}Si_{3.04}O_8$
Hornblende	48.0	1.26	6.8	13.9	0.39	14.0	11.5	1.4	0.6	—	97.8	nd
Biotite	53.4	2.22	14.9	8.0	0.40	6.1	4.8	2.2	6.0	—	96.8	nd
Smectite	48.9	0.93	25.4	10.6	0.01	1.3	0.5	0.1	0.6	—	88.2	nd
SCT 3												
Plagioclase	61.3	—	23.7	0.1	—	0.0	5.2	8.3	0.3	0.160	99.1	$Na_{0.72}Ca_{0.25}Al_{1.25}Si_{2.75}O_8$
K-feldspar	63.7	—	18.4	0.1	—	0.0	0.0	1.2	14.6	0.112	98.1	$K_{0.88}Na_{0.11}A_{11.02}Si_{2.99}O_8$
Biotite	32.0	3.05	16.4	23.0	0.19	4.2	0.1	0.1	5.2	—	84.5	nd
SCT 5												
Plagioclase	61.3	—	23.9	0.2	—	0.0	5.5	8.3	0.3	0.122	99.5	$Na_{0.70}Ca_{0.28}Al_{1.32}Si_{2.67}O_8$
K-feldspar	64.7	—	18.5	0.1	—	0.0	0.1	2.2	13.5	0.081	99.2	$K_{0.08}Na_{0.19}A_{11.01}Si_{2.99}O_8$
Biotite	36.5	2.60	18.0	15.6	0.16	8.6	0.3	0.2	5.0	—	87.4	nd
Purimisa formation												$Mg_{0.16}Ca_{0.14}Na_{0.12}K_{0.04}(Fe_{0.79}Al_{1.2}$
Smectite	48.9	0.00	20.7	14.7		1.7	0.5	0.9	0.5		87.8	$Mg_{0.02})Si_{3.47}Al_{0.53}O_{10}(OH)_2$

[a] Indicative of total Fe.

In situ weathering further increases the concentrations of inert quartz at the expense of other more weatherable primary minerals. For example, residual quartz in the SCT 3 terrace progressively increases with decreasing depth in both the Santa Margarita Sandstone and in the overlying terrace deposit (Fig. 3A). In contrast, more weatherable plagioclase shows a corresponding decrease with decreasing depth. The relative weatherability of each of these minerals is also shown in a thin section SEM photo (Fig. 3B) in which quartz remains essentially pristine while plagioclase has become highly pitted and porous.

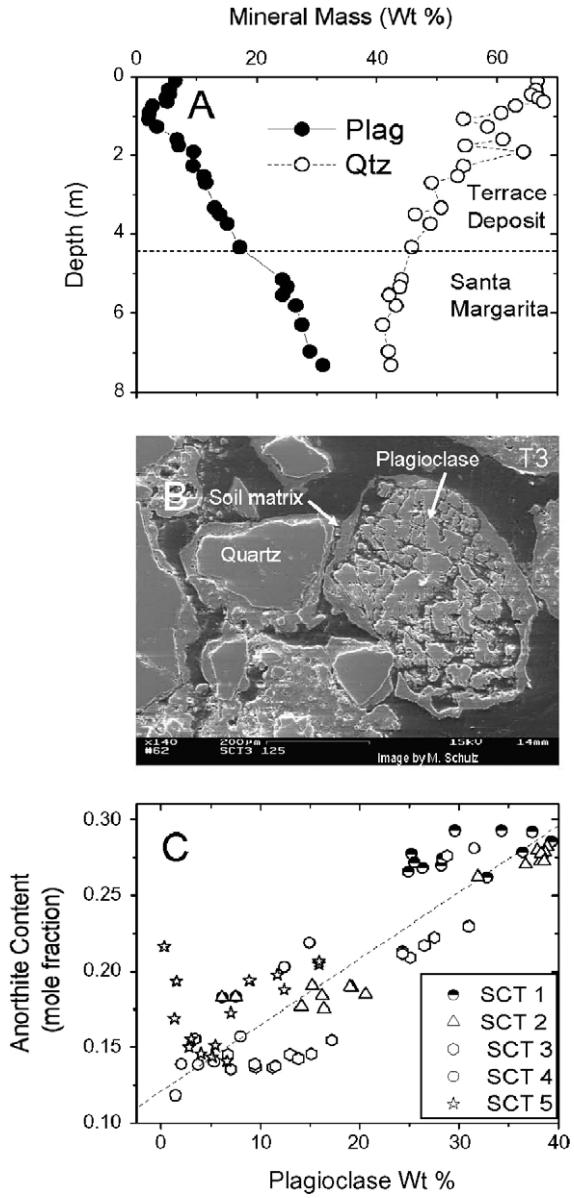

Fig. 3. Selective mineral weathering. (A) Quartz and plagioclase distributions as functions of depth in the SCT 3 terrace. Dashed line is the contact between the terrace deposit and Santa Margarita Sandstone. (B) SEM photograph showing the selective weathering of plagioclase relative to quartz (1.3 m depth in SCT 3). (C) Selective loss by weathering of the calcic component of plagioclase with decreasing residual plagioclase content in the terraces.

The calcic component of plagioclase is being selectively removed by weathering relative to the sodic component, both at progressively shallower depths in individual terraces and in sequentially older terraces (Fig. 3C). These data are based on the relative abundances of albite, oligioclase, and andesine in the bulk samples as determined by quantitative XRD, and by the approximate average anorthite contents of these phases (An_0, An_{20} and An_{40}, respectively; Deer et al., 1985). Such selective weathering may involve a range of grains of differing composition or, alternately, weathering of heterogeneities such as the calcic cores of individual plagioclase grains (Clayton, 1986).

In spite of stoichiometric variability, significant correlations exist between elemental and mineral weathering

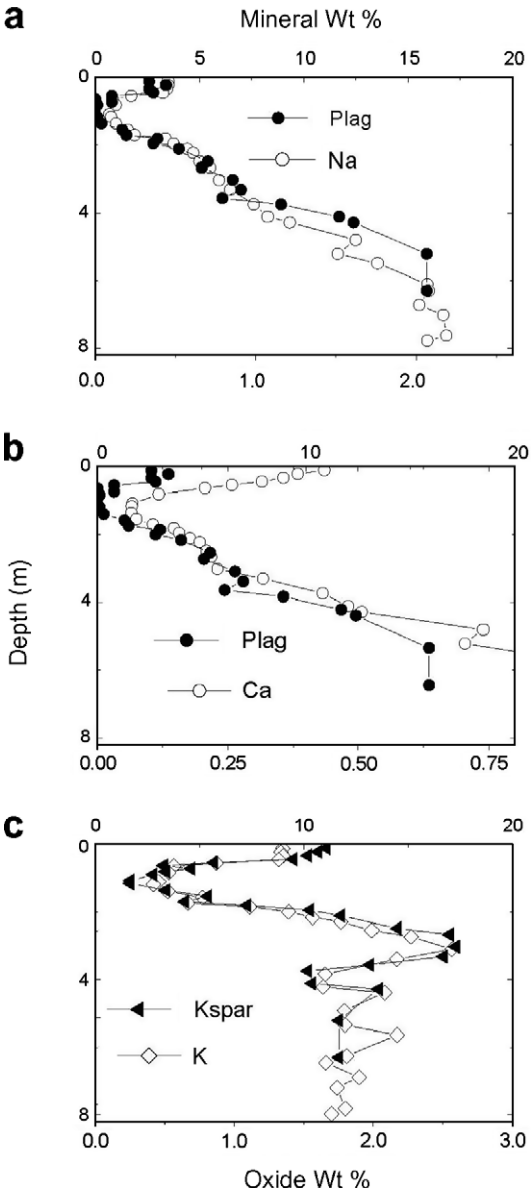

Fig. 4. Comparison of mineral and element distributions in the SCT 5 terrace. (a) Na and plagioclase, (b) Ca and plagioclase, and (c) K and K-feldspar. Upper axis in each plot corresponds to wt % of mineral and lower axis to wt% of oxide.

profiles in the terraces as shown for the concurrent losses of plagioclase and Na and Ca with decreasing depths in SCT 5 profile (Fig. 4a and b). As expected, K distributions in the profiles correlate with those of K-feldspar (Fig. 4c).

Mica phases, primarily biotite (Table 2), are present in terrace deposits but at concentrations lower than in the Ben Lomond Granite (Appendix I). Bradley (1957) observed that mica was heterogeneously distributed in terrace deposits, being preferentially deposited with fine grained neritic sediments relative to the coarser beach sediments. The present study found that micas were most abundant in the younger terraces near the basal horizons overlying the Santa Cruz Mudstone and Santa Margarita Sandstone. Hornblendes were also observed in thin sections taken of sediments from the younger terrace deposits and were analyzed by electron microprobe (Table 2). Older terrace deposits generally lacked hornblende.

3.3. Clay and Fe oxide distributions

Both smectite and kaolinite occur in the terrace regoliths (Appendix I). Maximum smectite concentrations occur in the lower two-thirds of the youngest SCT 1 terrace and at the base of the SCT 2 terrace (Fig. 5). Smectite is significantly diminished in the older terraces. XRD analyses of the $<0.2\,\mu m$ fraction of a sample from the base of the SCT 2 terrace indicated a mixture of both dioctahedral Fe-smectite and fine-grained, poorly crystalline kaolinite. The poorly defined XRD peak shapes and positions made it difficult to determine whether the kaolinite formed by direct precipitation of small discrete crystals or by the alteration of the smectite to a kaolinite/smectite mixed-layer structure.

The Santa Margarita Sandstone and Santa Cruz Mudstone are deficient in smectite and no measurable smectite is present in modern Wilder Beach sands. However, the Purisma Formation, which overlies the Santa Cruz mudstone (Fig. 1C) and crops out in local sea cliffs, contains "authigenic Fe-rich morillonoid cements of a distinctly blue color" (Lerbeko, 1956). XRD and XRF analyses of the $<0.2\,\mu m$ size fraction of a sea cliff Purisma sample obtained near the SCT 1 site (Fig. 1A) produced an almost pure di-octahedral Fe-smectite. The smectite stoichiometry, as determined by bulk XRF analyses, is reported in Table 2.

Extensive submarine exposures of the Purisma Formation occur on the adjoining continental shelf (Anima et al., 2002). The present study found Fe-rich smectite to be the principal clay (16 wt%) in a marine core taken on the continental shelf adjacent to the study area. These results imply that the Purisma Formation provides a significant source of smectite to the off-shore sediments and ultimately to the neritic component of the terrace deposits.

Kaolinite abundances increase with terrace age, becoming more concentrated in argillic horizons at depths of 0.5–1.5 m (Fig. 5). Similar argillic horizons are reported for many older soils developed in the Mediterranean climate of California (Torrent and Nettleton, 1978; Hobson and Dahlgren, 1998; White et al., 2005). XRD analyses indicate that kaolinite grain size and crystallinity does not increase with age in the Santa Cruz terraces.

The clay distributions shown in Fig. 5 imply that kaolinite is a secondary weathering product of the smectite that was originally deposited on the Santa Cruz terraces. A reaction, based on the smectite stoichiometry is (Table 2)

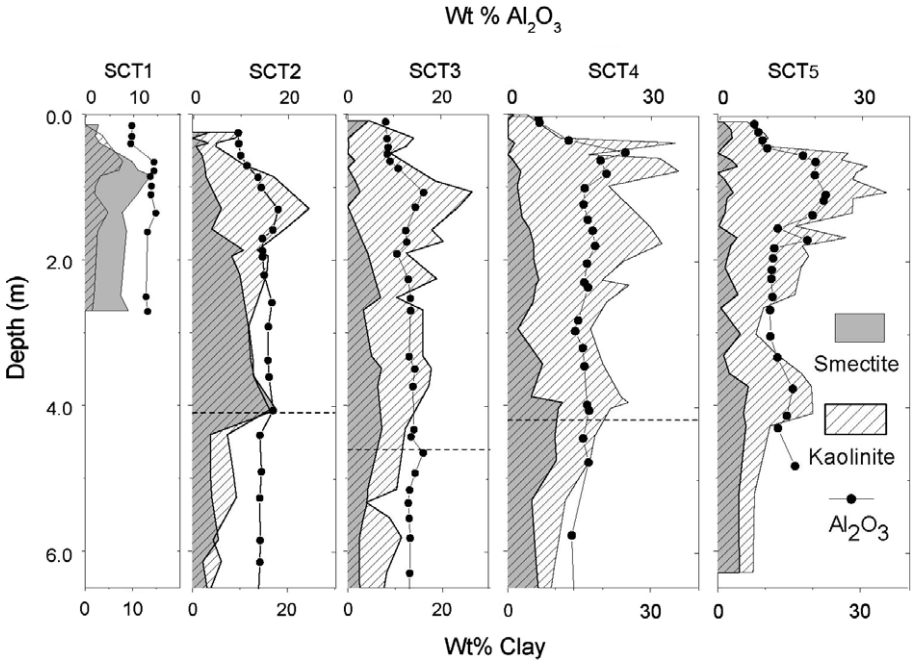

Fig. 5. Kaolinite and smectite (lower horizontal axes) and Al (upper horizontal axes) distributions as functions of depth in the terraces. Dashed lines are approximate contacts between the terrace deposits and the Santa Margarita Sandstone in SCT 2, SCT 3 and SCT 4.

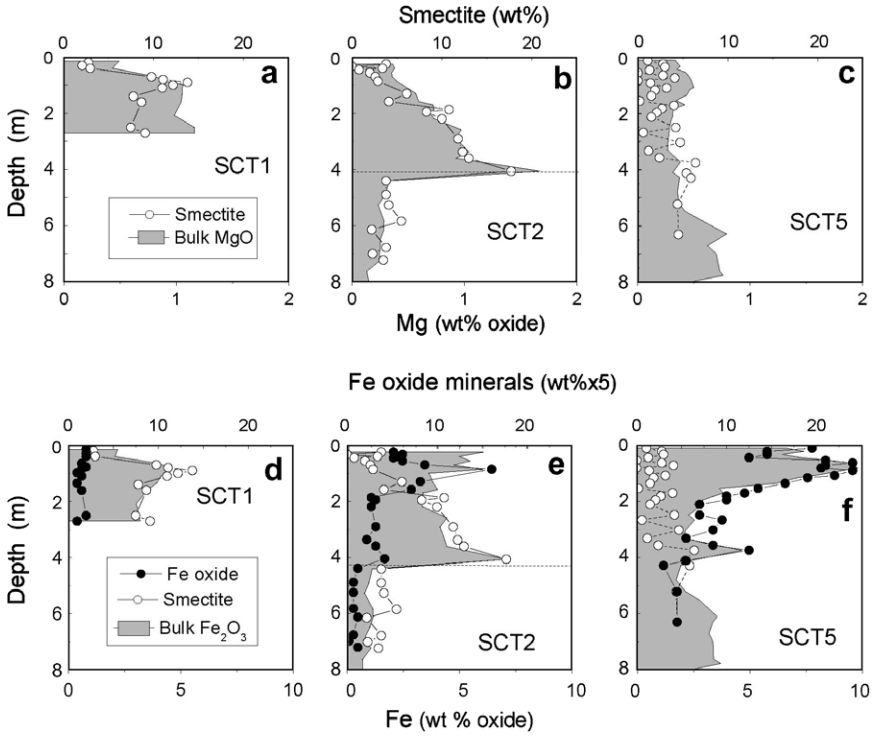

Fig. 6. Comparisons of clay and elemental distributions in the SCT 1, SCT 2 and SCT 5 terraces. (a–c) Mg and smectite distributions. (d–f) Fe, smectite and secondary Fe oxides. Dashed lines correspond to approximate contact between the SCT 2 terrace deposits and Santa Margarita Sandstone.

$$\begin{aligned} &Mg_{0.17}Ca_{0.04}Na_{0.12}K_{0.04}(Fe_{0.79}Al_{1.2}Mg_{0.02})Si_{3.47}Al_{0.53}O_{10}(OH) \\ &\quad(\text{smectite}) + 0.62H^+ + 3.90H_2O \\ &\quad\rightarrow 0.865Al_2Si_2O_5(OH)_4\ (\text{kaolinite}) \\ &\quad + 0.39Fe_2O_3(\text{Fe oxide}) + 0.19Mg^{2+} \\ &\quad + 0.04Ca^{2+} + 0.12Na^+ + 0.04K^+ + 1.74H_4SiO_4 \qquad (1) \end{aligned}$$

where the weathering of smectite concentrates Al and Fe in kaolinite and Fe-oxides and releases cations, principally Mg, to solution. Additional kaolinite is produced from the weathering of other primary silicates, mainly feldspars.

Changes in elemental concentrations, associated with clay weathering, generally mimic the distributions predicted by Eq. (1). Mg is highest in the youngest terraces and decreases in the older terraces, reflecting progressive losses during smectite weathering (Fig. 6a–c). Solid Al and Fe distributions are more complex because they are affected both by the weathering of detrital smectite and the formation of secondary kaolinite and Fe oxides Eq. (1). The high Al content in kaolinite accounts for the significant increases in Al in the argillic horizons in terraces of increasing age (Fig. 5). Like kaolinite, Al is depleted in the shallowest soil horizons probably due to its increased solubilities in CO_2- and organic-rich pore waters and/or as the result of downward clay illuviation.

In the youngest SCT 1 terrace with only minor Fe oxides, bulk elemental Fe, like Mg, closely correlates with the smectite distribution (Fig. 6d). While this correlation persists at depth in SCT 2 (Fig. 6e), Fe also increases in the shallow argillic horizon, implying transfer from smectite to Fe oxide minerals. In the oldest, most intensely weathered SCT 5 profile, residual smectite is low and bulk Fe is almost exclusively associated with Fe-oxides in the argillic horizon (Fig. 6f).

At shallow terrace depths (<0.5 m), up to half of the total Fe occurs in nodules >2 mm in diameter (Fig. 7A). These nodules, the abundance of which increases with terrace age, consist principally of Fe oxides cementing silicate grains. The SEM backscatter image in Fig. 7B shows an example of the complex structure of a nodule where zones of higher Fe content are distributed as bright bands around a quartz grain, suggesting successive episodes of Fe oxide precipitation. The nodules are a mixture of goethite and maghemite (Fig. 7C).

At depths between 0.5 and 1.0 m, the nodules become less abundant and disseminated Fe in the <2 mm fraction substantially increases (Fig. 7A). This Fe commonly coats silicate mineral grains but does not produce coherent cement exemplified in the nodules. The highest disseminated Fe concentrations occur at the top of the argillic horizon (1 m), the heterogeneous distributions of which produce intense red/gray mottling in the older terraces. Goethite is the major disseminated Fe-oxide phase (Fig. 7C).

4. DISCUSSION

Elemental and mineral distributions in the present Santa Cruz chronosequence, compared to those of the initial sediments, reflect the effects of long-term weathering. The present discussion will define these differences in space and time

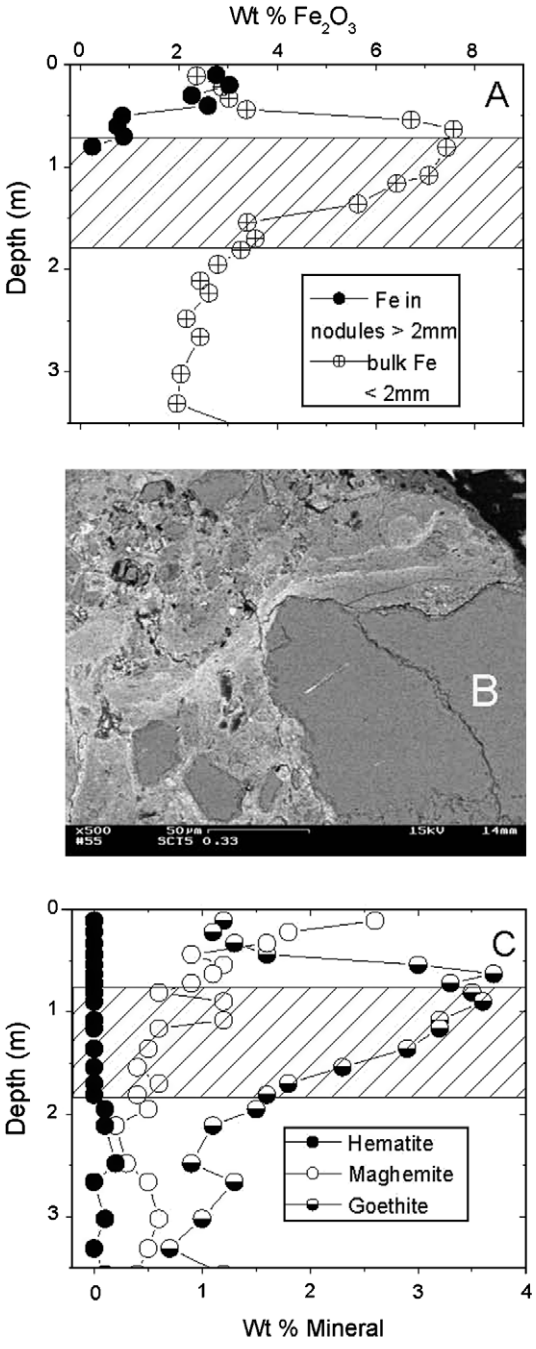

Fig. 7. Fe oxide distributions in Terrace SCT 5. (A) Distributions of Fe in nodules and disseminated oxides. (B) Backscatter SEM photograph showing heterogeneous Fe distributions (light colors) in nodule at 0.3 m depth. (C) Secondary Fe mineral distributions. Hatched areas are the approximate extent of the argillic horizon.

and will provide insights into the mechanisms and rates responsible for their evolution.

4.1. Elemental mobilities

One of the simplest approaches in describing weathering intensity is to directly compare ratios of present day element, mineral or isotope concentrations to those of the original protolith, i.e., $C_{j\mathrm{w}}/C_{j,\mathrm{p}}$, This ratio is dependent upon not only the weatherability of component j but also on gains and losses of other components in the regolith and on compaction or dilation of the soil or regolith. Overcoming such effects requires comparing the ratio of the mobile component j to the ratio of an additional inert component i,

$$\tau_j = \frac{C_{j,\mathrm{w}} \cdot C_{i,\mathrm{p}}}{C_{j,\mathrm{p}} \cdot C_{i,\mathrm{w}}} - 1, \tag{2}$$

τ_j is defined as the mass transfer coefficient (Brimhall and Dietrich, 1987) and is comparable to other derivations such as the chemical depletion factor of Riebe et al. (2003). A values of $\tau_j = 0$ denotes no mobility, while $\tau_j = -1$ indicates complete mobility and $\tau_j > 0$ denotes external additions.

Regolith volume change or strain ε_i is an additional parameter dependent on the ratio of the weatherable to inert components (Brimhall and Dietrich, 1987)

$$\varepsilon_i = \frac{\rho_{\mathrm{p}} C_{i,\mathrm{p}}}{\rho_{\mathrm{w}} C_{i,\mathrm{w}}} - 1, \tag{3}$$

where ρ_{p} and ρ_{w} are the respective protolith and regolith densities (g cm^{-3}). A value of $\varepsilon_i = 0$ is indicative of isovolumetric weathering while $\varepsilon_i > 0$ indicates regolith expansion and $\varepsilon_i < 0$ signifies regolith collapse.

Refractory elements such as Zr, Ti and Nb are commonly used as conservative components, C_i in Eqs. (2) and (3) (Brimhall et al., 1991; Merritts et al., 1991; White et al., 1998; Riebe et al., 2001). However, in depositional environments such as Santa Cruz, these elements are susceptible to density segregation due to their presence in heavy minerals (White et al., 1996). Concentration and winnowing of such minerals are clearly evident as dark-colored magnetite/ilmentite bands distributed across the surface of present day Wilder Beach. Such heterogeneities explain the large concentration ranges of Zr and Ti in the beach sands (Appendix I).

An alternate approach is to use quartz as the inert component (C_i in Eqs. (2) and (3)). Quartz has long been considered an indicator of weathering intensity (Ruhe, 1956) and used as a conservative component in mass balance calculations (Sverdrup and Warfvinge, 1995; White et al., 1996). Due to similar grain sizes and densities, quartz, unlike heavy minerals, behaves similarly to more reactive aluminosilicates such as feldspars in depositional environments. Although quartz does weather, its rate in most weathering environments is slow compared to aluminosilicates. The resulting quartz strain estimates for SCT 2 and 3 (Fig. 8a) generally mimic feldspar distributions in which the zone of maximum weathering (Fig. 3A) corresponds to the zone of maximum volume collapse in the argillic horizon (Fig. 8a). The loss also occurs in regolith horizons with the highest bulk densities (Fig. 8b).

4.1.1. Protolith compositions

Unlike for the case of in situ weathering, the Santa Cruz protoliths defined in Eqs. (2) and (3) do not reflect unweathered bedrock, but rather the compositions of sediment that has been previously weathered. Terrace

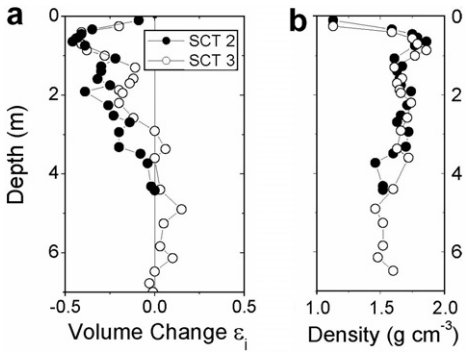

Fig. 8. Volume changes (ε_i in Eq. (3)) and measured bulk density distributions) in the SCT 2 and SCT 3 profiles (Appendix I).

protoliths can be equated with contemporary beach deposits as done for the Mattole and Jughandle marine terraces (Brimhall and Dietrich, 1987; Chadwick et al., 1990). However in the Santa Cruz study, Wilder Beach sands do not serve as a direct analogue because of they do not incorporate the finer clay-rich offshore sediments that were present in the initial terrace sediments.

Weathering intensity commonly decreases with regolith depth. An alternative approach is to assume that deep terrace samples reflect the original pristine sediments as done in other chronosequence studies (White et al., 1996; Langley-Turnbaugh and Bockheim, 1998). The present paper utilizes more than a single terrace composition as the assumed protolith, an approach which considers differences in mineral weathering characteristics.

Protolith Na, Ca and Sr concentrations, reflecting plagioclase weathering (Group I elements in Table 3), were represented by the deepest samples in each terrace. For the SCT 1 and 5, they were obtained directly above the Santa Cruz mudstone. For SCT 2, 3 and 4, they were samples obtained within the underlying Santa Margarita Sandstone. Protolith K, Rb and Ba concentrations, reflecting shallower weathering of K-feldspar (Group II elements in Table 3) are represented by samples taken near the base of the each terrace deposit. Al, Fe, Mg concentrations reflect a wider range of weathering interactions dominated by the loss of smectite and formation of secondary kaolinite and Fe oxides). The protolith compositions for these Group III elements in all the terraces are assumed to be represented by the average composition of SCT 1 below a depth of 1 m (Table 3). The SCT 1 sediments contain relatively uniform distributions of detrital smectite which was assumed to have been initially present in all of the older terrace deposits.

4.1.2. Mobility of Na, Ca, Sr

The intensity of plagioclase weathering is reflected in the relative mobilities of Na, Ca, and Sr plotted as functions of τ_j with depth in Fig. 9. The vertical dashed lines correspond to zero mass mobility ($\tau_j = 0$) and intersect the assumed protolith composition at depths listed in Table 3. Using average sand compositions as the protolith (Table 3), present day Wilder beach exhibits small random differences in

Table 3
Protolith parameters used to calculate mass transfer coefficients and strain Eqs. (2) and (3)

	Beach	SCT 1	SCT 2	SCT 3	SCT 4	SCT 5
	Group I					
Na_2O	1.74	2.95	1.95	2.26	2.74	2.61
CaO	2.62	2.14	1.91	1.33	2.41	1.82
SrO	0.025	0.035	0.038	0.037	0.038	0.025
Depth (m)	Average	2.70	10.06	11.52	9.00	9.45
Qtz	nd	42.1	44.0	42.0	42.8	56.1
Density[c]	1.65	1.71	1.40	1.60	1.52	1.61
	Group II					
K_2O	1.41	1.93	2.02	1.66	2.50	1.64
Rb_2O	0.0043	0.0068	0.0078	0.0103	0.0094	0.0062
BaO	0.047	0.079	0.093	0.121	0.103	0.074
Depth (m)	Average	2.70	3.60	4.42	4.04	4.11
Qtz	nd	42.1	33.6	45.0	45.9	48.6
Density[c]	1.65	1.71	1.36	1.52	1.41	1.55
	Group III					
MgO	0.94	1.09	1.09	1.09	1.09	1.09
AI_2O_3	8.026	13.25	13.25	13.25	13.25	13.25
Fe_2O_3	2.89	3.56	3.56	3.56	3.56	3.56
SiO_2	80.5	75.2	75.2	75.2	75.2	75.2
Depth (m)	Average[a]	Average[b]	Aver.[b]	Average[b]	Average[b]	Average[b]
Qtz	nd	40.0	40.0	40.0	40.0	40.0
Density[c]	1.65	1.68	1.68	1.68	1.68	1.68

Data as wt% except as noted.
[a] Average beach compositions, 0–3.1 m depth.
[b] Average of lower half of SCT 1, 1.1–2.7 m depth.
[c] Density as g cm^{-3}.

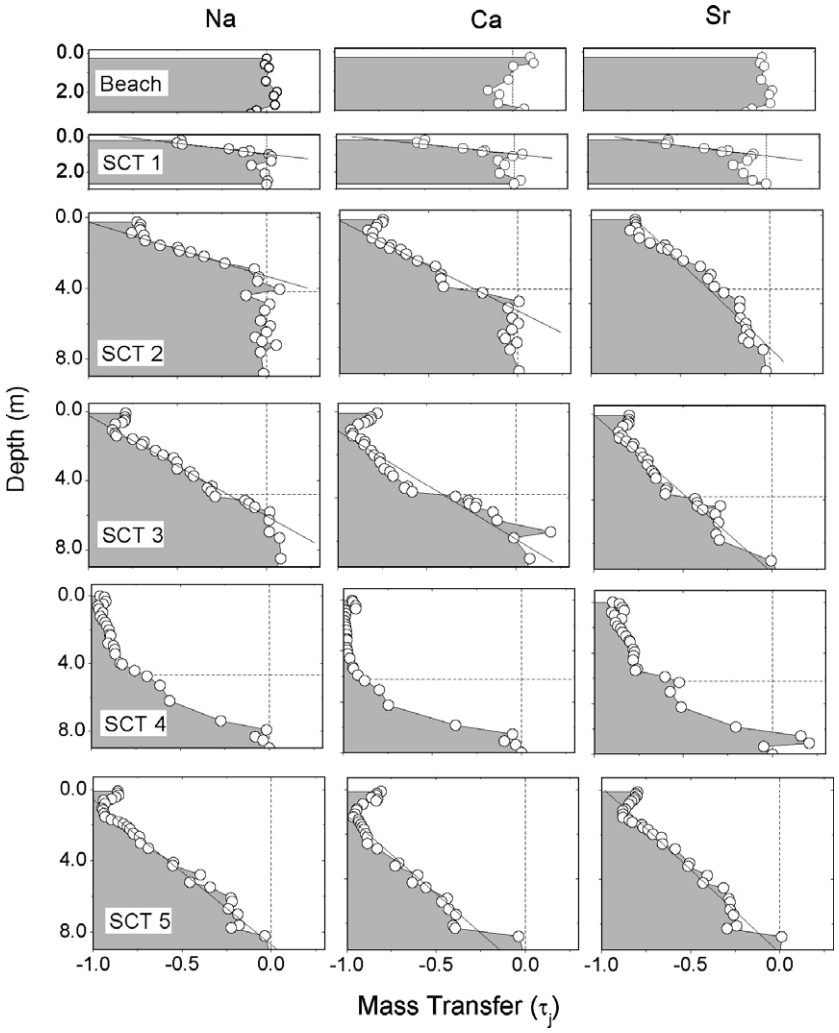

Fig. 9. Na, Ca, and Sr mobilities (τ_j, values from Eq. (2)) in the Santa Cruz terrace profiles, including Wilder Beach. Diagonal lines are linear least square fits used to isolate eolian inputs (Table 4). Vertical dashed lines denote no mobility and horizontal dashed lines the contact between the terrace deposit and the Santa Margarita Formation.

Na, Ca and Sr that reflect depositional variations in plagioclase with depth.

Na, Ca, and Sr mobilities in the terrace deposits are strongly dependent on regolith depth and age (Fig. 9). A maximum loss of 50% Na, Ca and Sr ($\tau_j = -0.5$) occurs at a depth of 0.3 m in SCT 1. The weathering profile, denoted by progressive increasing τ_j values, extends downward to 1 m. The terrace sediments below this depth are essentially unweathered, reflecting the original protolith. In the slightly older SCT 2 terrace, maximum Na, Ca and Sr depletions of 80% occur at 1 m. Weathering in this profile extends downward to near the contact with the underlying Santa Margarita Sandstone (Fig. 9; horizontal dashed line at 4 m).

The weathering patterns in SCT 2 and older terraces are element specific. Na is the least depleted, Ca is moderately depleted and Sr is the most depleted. These elemental differences reflect heterogeneous weathering of plagioclase (Fig. 3C). Experimental studies have documented the initial non-stoichiometric release of Sr > Ca > Na from plagioclase due to preferential leaching of surfaces and exsolution lamellae (Brantley et al., 1998).

In the older SCT 3 and 4 terraces, Na, Ca and Sr losses extend deeper into the unconsolidated Santa Margarita Sandstone. Consistency in elemental mobilities across these contacts indicates that for plagioclase, the terrace deposits and underlying Santa Margarita sandstone function as single weathering units. This result is not unexpected because sands contained in both formations were derived from the same local plutonic rocks in the Santa Cruz Mountains (Perg et al., 2003). This conclusion is further supported by similarities in $^{87}Sr/^{86}Sr$ data to be described elsewhere. The weathering profile in the oldest SCT 5 regolith (225 kyrs) is similar to SCT 4 but is confined exclusively to deeper terrace deposits.

4.1.3. Mobility of K, Rb and Ba

The Wilder Beach sand τ_j values exhibit only minor variations for K, Rb, and Ba with depth which reflect consistent amounts of K-feldspar (Fig. 10). The mobilities of

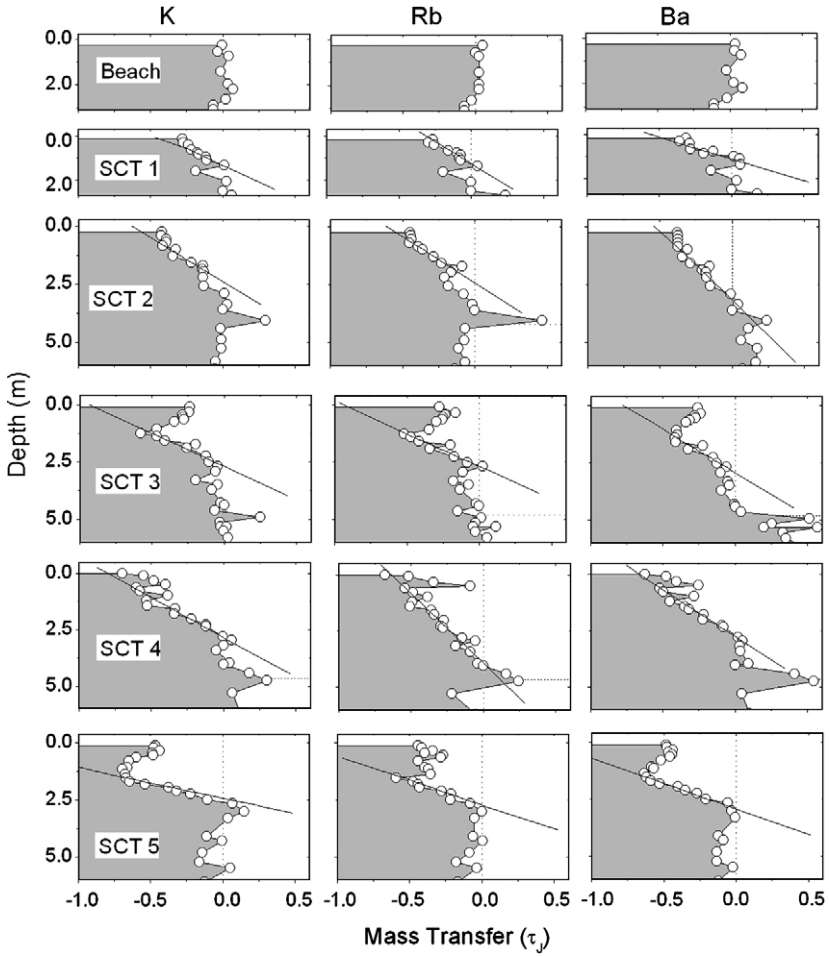

Fig. 10. K, Rb and Ba mobilities (τ_j values from Eq. (2)) in the Santa Cruz terrace profiles, including Wilder Beach. Diagonal lines are linear least square fits used to isolate eolian inputs (Table 4). Vertical dashed lines denote no mobility and horizontal dashed lines the contact between the terrace deposit and the Santa Margarita Formation.

these elements are extended to increasing depths in the SCT 1 and SCT 2 profiles (1.4 and 2.8 m, respectively) but remain relatively constant thereafter in SCT 3, SCT 4 and SCT 5 terraces (2.7–2.9 m). These elemental profiles are confined to the terrace deposits with no evidence of K-feldspar weathering in the underlying Santa Margarita sandstone (Fig. 10).

Lesser mobilities of K, Ba and Rb, relative to Na, Ca and Sr, reflect slower weathering of K-feldspar relative to plagioclase, a commonly observed phenomenon (Nesbitt and Young, 1984; White et al., 2001). Additional K, Rb and Ba occur in illite/mica and smectite, accounting for the anomalously high residual τ values in the basal units of SCT 2, SCT 3 and SCT 4 (Fig. 10; also see mineral distributions in Appendix I). Due to this heterogeneity, the initial protolith K, Rb, and Ba concentrations were taken to be at depths immediately above the basal zones of the terrace deposits (Table 3).

4.1.4. Effect of eolian deposition on weathering profiles

Shallow soil horizons, particularly those in the older terraces, exhibit enrichment of specific elements above about 1 m. These reversals are most apparent for K, Rb and Ba distributions in the SCT 3 and 5 terraces (Fig. 10) but also occur for Na, Ca and Sr (Fig. 9). Surficial concentration implies relatively recent external inputs, most likely from eolian deposition. Long distance transport of Asian dust probably contributes minerals containing alkaline and alkaline earth elements to coastal areas of California although their fluxes are not well characterized (Leinen et al., 1994).

Local eolian sources in vicinity of the Santa Cruz terraces are currently limited to sand derived from relatively narrow beaches confined by steep sea cliffs. However, bathymetry data (Eittreim et al., 2002) indicate that a drop in sea level of 120 m occurred during the last glacial maximum (22 kyrs ago) exposing the entire continental shelf to a distance of some 15 km west of the current coastline (Fleming et al., 1998). Extensive eolian transport and deposition during this period is evidenced today in paleo-sand dunes in low lying areas to the south along Monterey Bay (Dupre et al., 1980). Eolian deposition on marine terraces resulting from exposure of the continental shelf during the Pleistocene is also found in Southern California (Muhs, 1992).

The relative young age of the eolian deposits minimizes the extent of subsequent in situ weathering. However, the relative increase in surficial K-feldspar relative to

plagioclase suggests the some selective weathering has occurred. Concentration and mobility reversals appear to be greater in the other older terraces because eolian deposition occurred on surfaces that were more depleted in feldspars by previous long-term weathering, thus increasing the concentration contrasts. Shallow elemental enrichment is not observed for SCT 4 terrace because of the stripping of the surface horizons by human activities.

4.1.5. Mobility of Mg, Al, and Fe

The mobilities of Mg, Al and Fe in the terrace profiles are very different than for cations controlled principally by feldspar weathering. Due to its ubiquitous presence in silicate minerals, Al is neither enriched nor depleted in the present day Wilder Beach sands ($\tau_{Al} \approx 0$ in Fig. 11). In contrast, Mg and Fe are significantly enriched in the basal sands due to the preferential concentration of biotite. Retention of Fe, Mg and Al in SCT 1 reflect residual smectite (Fig. 5). The apparent enrichments in the basal horizon of SCT 2 (Fig. 11) also correspond to smectite concentrations significantly in excess of those in the lower half of SCT 1, the assumed protolith composition (Table 3).

Significant Mg losses in the older SCT 3, 4 and 5 terraces (Fig. 11) correlate with the depletion of smectite (Eq. (1) and Figs. 5 and 6). While Al and Fe are also mobilized by smectite weathering, these elements are not lost from the terrace profiles but are significantly concentrated relative to the protolith in kaolinite and Fe oxides in the shallow argillic horizons (Fig. 11).

Aluminum and particularly Fe enrichments are described for argillic horizons in other marine terrace chronosequences. Langley-Turnbaugh and Bockheim (1998) proposed that high Fe concentrations in argillic zones were derived from inflow of Fe-enriched water from topographically higher terraces. This is unlikely at Santa Cruz due to hydrologic isolation of the upper terrace horizons from significant lateral ground water flow. Likewise, internal redistribution by illuviation (Buol et al., 2003) or concentration due to regolith collapse ($\varepsilon_i < 0$ in Eq. (3); Brimhall and Dietrich, 1987) are not likely scenarios for Fe enrichment of the argillic horizons.

The problem of Fe redistribution in the Santa Cruz terraces is not related to finding a source which is in the initially abundant detrital smectite Eq. (1). Rather it is how,

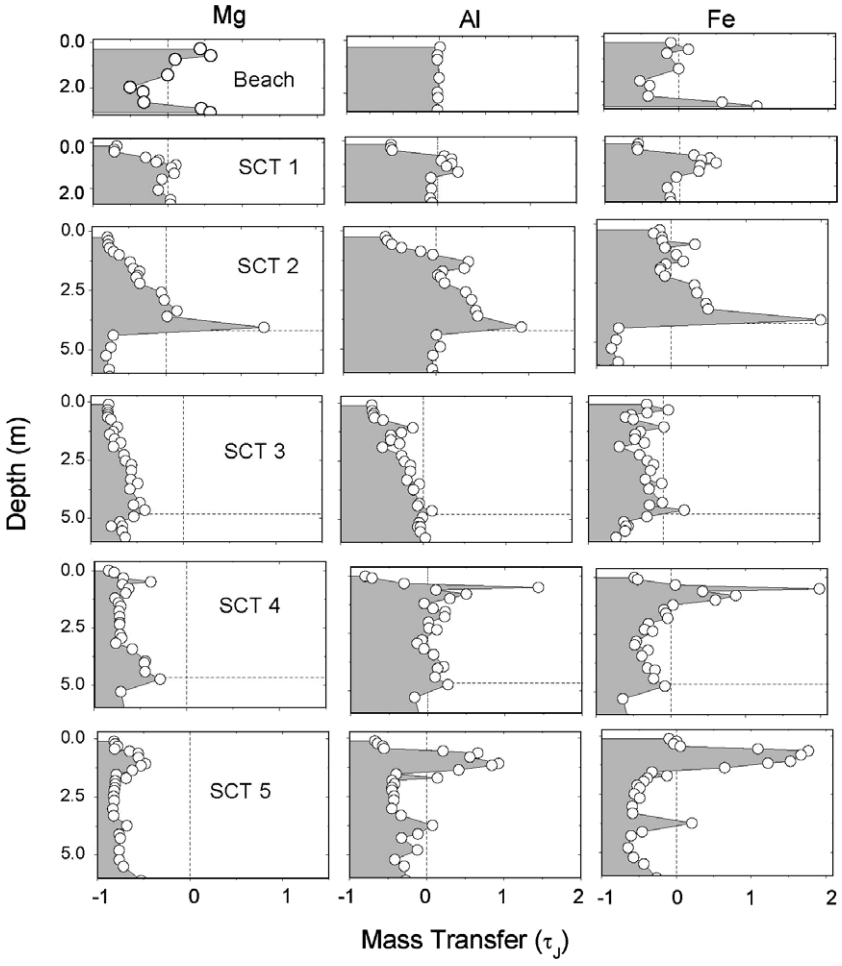

Fig. 11. Mg, Al and Fe mobilities (τ_j values from Eq. (2)) in the the Santa Cruz terrace profiles, including Wilder Beach. Vertical dashed lines denote no mobility and horizontal dashed lines the contact between the terrace deposit and the Santa Margarita Formation.

during weathering, Fe was mobilized upward and concentrated in the relatively shallow argillic horizons. One possibility is that such transport is facilitated by active bio-pumping by vegetation. The annual uptake of Fe by the present day grasslands, when extrapolated on the age of the terraces, is greater that the total Fe in the shallow soil. While other mineral nutrients, such as Ca and Mg, are readily solubilized during plant growth and decay, a portion of the Fe may be sequestered as insoluble secondary Fe oxides. With time, this Fe may be expected to gradually build up in the argillic horizon (Figs. 6 and 11). The interconnection between weathering and biology will be discussed in greater detail in a subsequent paper.

4.1.6. Mass changes

The total mass of a component j weathered from the regolith ΔM_j (mol), normalized to unit soil surface (m^2) and measured over a profile depth interval z (m), is described by the relationship (Chadwick et al., 1990)

$$\Delta M_j = \left(\rho_p \frac{C_{j,p}}{m_j}\right) \int_{z=0}^{z=d} \tau_j \, dz \quad (4)$$

where ρ_p is the protolith density and m_j is the atomic weight of species j. The above expression has been used in a large number of weathering studies including those involving marine terraces (Merritts et al., 1992; Langley-Turnbaugh and Bockheim, 1998).

The total elemental changes ΔM_j in each of the Santa Cruz terrace profiles are listed in Table 4. Data in parentheses are net changes in elements after subtracting out additions from recent eolian deposition for Group I and II elements. These corrections were made by projecting least squares fits to the mass transfer coefficients τ_j through the inflection points reflecting the onset of the eolian input above 1 m (diagonal lines in Figs. 9 and 10). No corrections were made for the SCT 4 terrace due to the absence of an upper soil horizon.

Table 4 indicates that removing the eolian input marginally increases mass losses of Na, Ca and Sr due to weathering. In contrast, this correction substantially increases K, Rb and Ba mobilities by almost 50% in the oldest terraces. Total elemental mass changes ΔM_j (after corrections for eolian deposition) are plotted with respect to terrace ages in Fig. 12. Na, Ca and Sr generally exhibit large and increasing losses with time (Fig. 12a). The only significant discrepancy is the greater mobilities of these elements in SCT 4 compared to the older SCT 5. The cause of this discrepancy is not certain but may be related to local effects involving higher rainfall amounts and a shallower water table at SCT 4. Much of the plagioclase weathering in SCT 4 also occurs within the Santa Margarita Sandstone while weathering in SCT 5 is confined solely to a deeper terrace regolith.

K, Ba and Rb losses also occur with increasing terrace age (Fig. 12b). However these losses are significantly less than for Na, Ca and Sr, reflecting the much slower weathering of K-feldspar relative to plagioclase. Mg, mobilized by smectite weathering, is also lost from the older profiles (Fig. 12c). In contrast, Al and Fe exhibit no consistent mass changes with time due to incorporation into kaolinite and Fe-oxides, principally in the argillic horizon.

4.1.7. Mass fluxes

The average long term weathering flux Q_i (mol yr^{-1}) is defined as

$$Q_j = \frac{\Delta M_j}{\Delta t} \quad (5)$$

where Δt (years) is the duration of weathering. Negative values of Q_j correspond to net output fluxes and positive values net input fluxes. Mass fluxes are a useful approach to compare weathering in different environments.

Table 4
Mass changes ΔM_j Eq. (4) associated with of the Santa Cruz terraces (mol m^{-2})

	Beach	SCT 1	SCT 2	SCT 3	SCT 4	SCT 5
	Group I					
Na	24	−458 (−506)	−2020 (−2230)	−3020 (−3140)	−7117	−5510 (−5600)
Ca	−43	−240 (−270)	−1370 (−1450)	−1290 (−1370)	−4000	−2715 (−2760)
Sr	0	−0.0040 (−0.00430)	−0.0093 (−0.0096)	−0.015 I (−0.0154)	−0.0570	−0.0179 (−0.0183)
Interval (m)		0.0–2.70	0.0–10.1	0–11.5	0–9.0	0–9.45
	Group II					
K	3	−275 (−296)	−499 (−528)	−478 (−700)	−676 (−762)	−452 (−772)
Rb	0.0002	−0.0040 (0.0039)	−0.0068 (−0.0071)	−0.0049 (−0.0082)	−0.0103 (−0.0117)	−0.0048 (−0.0102)
Ba	−0.000	−0.001 (−0.0002)	−0.0013 (−0.0015)	−0.0032 (−0.0035)	−0.0041 (−0.0047)	0.0048 (−0.0074)
Interval (m)		0–2.70	0–3.60	0–4.42	0–4.04	0–4.11
	Group III					
Si	363	−1940	2400	−19600	−9250	−19700
Fe	−146	−89	1068	−607	−244	371
Al	38	−758	3680	−4930	2440	−3040
Mg	−92	−179	−278	−1340	−1330	−1760
Interval (m)		0–2.70	0–3.60	0–4.42	0–4.04	0–4.11

Data in parentheses exlude additions from eolian deposition.

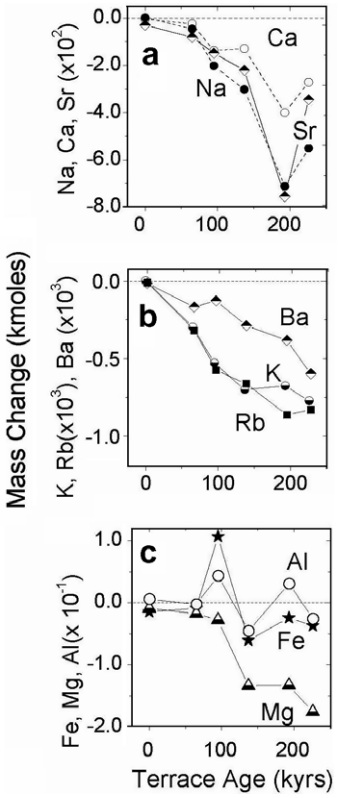

Fig. 12. Total mass changes ΔM_j due to weathering of the Santa Cruz terraces including Wilder Beach from Eq. (4). Negative values denote mass losses and positive values net gains (note differences in element scales on vertical axes). Elements in (a) and (b) are corrected for eolian inputs.

Elemental fluxes for the Santa Cruz chronosequence, in addition to other marine terraces along the Pacific Coast of California, are tabulated in Table 5. Also included are terrace depths and ages, the nature of the protolith and average annual precipitation. Due to the significant difference in terrace thicknesses, chemical fluxes Eq. (5) are normalized to a unit depth (1 m).

Fluxes of Ca, Na and K, dominated by feldspar weathering, are negative for Santa Cruz and are comparable in magnitude to those of the other marine chronosequences. Mg fluxes are also negative, reflecting principally smectite weathering at Santa Cruz and probably hornblende and/or biotite weathering in the other chronosequences. In contrast, the magnitudes of Fe fluxes are small compared to the amounts of total Fe present, implying general retention in the regoliths.

Comparisons of elemental fluxes are potentially useful in evaluating external effects, such as climate, on weathering. As shown in Table 5, average annual rainfall is a significant variable along the Pacific Coast, ranging from 190 cm in Oregon to 30 cm in southern California. A correlation between rainfall and increased Ca and Na fluxes is suggested, particularly for the younger terraces. A more definitive climatic comparison for the Pacific Coast marine terraces would require additional data, particularly from drier, more southerly terraces sequences.

4.2. Mineral weathering rates

As indicated in the previous discussion, strong correlations exist between elemental distributions in the Santa Cruz profiles and the weathering of specific minerals phases, including plagioclase, K-feldspar and smectite (Figs. 4–6). Several different approaches are now discussed that relate mineral weathering to profile development.

The simplest definition for mineral weathering rate R (mol m^{-2} s^{-1}) is

$$R = \frac{\Delta M}{S_v \cdot \Delta t} \tag{6}$$

which is similar to elemental flux previously described in Eq. (5). The difference is that R is normalized against the total surface area of a specific mineral contained in a volume of regolith ($S_v = m^2\ m^{-3}$). This is essentially a "black box" approach which does not consider the spatial distributions of the minerals.

Alternately, weathering rates can be interpreted based on the mineral distributions with depth such as shown for the plagioclase and K-feldspar weathering profiles in Fig. 4. This geometric approach defines R as (White et al., 2001; White, 2002)

$$R = \frac{\omega}{b_s \cdot S_v}. \tag{7}$$

The term ω (m s^{-1}), shown in the schematic in Fig. 13 is the weathering velocity, which in the absence of physical erosion, is the rate at which the weathering front propagates into the protolith. The slope of the weathering profile or gradient b_s is the ratio of change in mineral concentration to change in regolith depth (m). When using the common convention of plotting depth as the vertical ordinate axis (Fig. 13), b_s is defined in terms of m per mol m^{-3}.

For steady state weathering conditions (R and ω are constants), the slope b_s and volumetric surface area S_v are inversely correlated Eq. (7). The slope of the profile becomes steeper as the volumetric surface area and the amount of residual mineral decreases toward the regolith surface. For changing weathering conditions, a faster mineral weathering rate R produces a shallower gradient b_s and a more rapid change in residual mineral concentration with depth. In contrast, a slower weathering rate produces a steeper gradient. Alternately, increases or decreases in the weathering velocity will increase or decrease the slope of the weathering gradient.

Weathering fluxes and gradients Eqs. (6) and (7) are empirical descriptions that do not consider mineral weathering in terms of the controlling mechanisms. A general form of a mechanistic rate expression at constant temperature is (Lasaga, 1998)

$$R = k_r \prod_j a_j^{m_j} f(\Delta G) \tag{8}$$

where the first right-hand term is the rate constant intrinsic to the mineral phase k_r (mol m^{-2} s^{-1}), the second term describes catalytic and inhibitory effects of aqueous species a_j, and the third term describes the response of the rate to the decline in excess free energy ΔG as the mineral dissolution

Table 5
Elemental mass fluxes (Q, Eq. (5)) for selected terrace chronosequences along the Pacific coast of the United States

Terrace	Age (kyrs)	Depth (m)	Precip. (m)	Q_{Na} (mmol m^{-3} kyr^{-1})	Q_{Ca} (mmol m^{-3} kyr^{-1})	Q_{K} (mmol m^{-3} kyr^{-1})	Q_{Mg} (mmol m^{-3} kyr^{-1})	Q_{Fe} (mmol m^{-3} kyr^{-1})
Santa Cruz, California[a]*; assumed protolith (see Table 3)*								
SCT 1	65	2.7	0.37	−2.30	−0.99	−0.56	−1.02	−0.51
SCT 2	90	4.1	0.52	−1.96	−1.33	−1.10	−0.75	3.51
SCT 3	137	4.4	0.61	−1.84	−0.76	−1.76	−2.22	0.70
SCT 4	194	4.0	0.69	−4.10	−2.30	−0.73	−1.71	0.37
SCT 5	226	4.0[f]	0.59	−2.58	−1.27	−1.02	−1.95	1.79
Cape Blanco, Oregon[b]*; protolith, base of Cape Blanco terrace*								
Cape Blanco	80	1.9	1.90	−5.39	−2.92	−1.64	−6.99	0.13
Pioneer	105	1.1	1.90	−5.16	−2.61	−1.30	−6.40	−1.36
Pioneer	105	1.4	1.90	−3.12	−1.12	−1.03	−4.48	−4.07
Silver Butte	125	2.1	1.90	−7.98	−3.08	−2.13	−6.18	−4.00
Indian Creek	240	3.4	1.90	−4.52	−1.73	−0.90	−3.90	−2.32
Indian Creek	240	5.4	1.90	−4.50	−1.67	−1.00	−3.76	−0.94
Mattole, California[c]*; protolith, beach*								
Pedon 1	3.6	1.2	1.00	−20.1	−11.6	nd	0.00	4.16
Pedon 2	29	1.3	1.00	−4.04	−1.46	nd	−1.96	−2.39
Pedon 3	40	1.4	1.00	−8.70	−2.45	nd	−2.79	−3.21
Pedon 4a	124	3.0	1.00	−1.65	−0.54	nd	−0.42	−0.48
Pedon 4b	124	2.8	1.00	−2.63	−0.62	nd	−0.45	−0.62
Strawberry	240	2.8	1.00	−1.20	−0.21	nd	−0.36	−0.03
Fort Bragg, California[d]*; protolith, beach*								
Jughandle	400	1.7	0.98	−0.89	−0.09	−0.50	nd	−0.09
Ventura California[e]*; protolith, base of Punta Gorda terrace*								
Punta Gorda	40	3.5	0.31	−3.13	−1.24	−0.74	1.11	2.66

Data normalized to unit depth.
[a] This study.
[b] Langley-Turnbaugh and Bockheim (1998).
[c] Merritts et al. (1992).
[d] Brimhall and Dietrich (1987).
[e] Harden et al. (1986).
[f] Only the upper 4.0 m is considered in flux.

approaches thermodynamic saturation. The parameters contained in Eq. (8) are generally not well-constrained for natural weathering environments.

4.2.1. A weathering profile calculator

The present discussion aims to characterize the basic controls on weathering that are responsible for producing the well-developed weathering profiles in the Santa Cruz terraces (Fig. 4). The approach will focus on parameters that can be interpreted from field-based weathering studies and will employ a "*weathering profile calculator*" based on a modified EXCEL spreadsheet previously used to describe permeability-limited weathering in granite-saprolite weathering profiles (White et al., 2001). A partial calculation describing the SCT 5 plagioclase weathering profile, using this approach, is contained in Appendix II.

The calculator uses very limited solute inputs and, as such, represents significant simplification of the more complex aspects of weathering addressed in Eq. (8) and those described by modeling simulations that couple solute compositions, fluid transport and, increasingly, the impacts of biology (Lichnter et al., 1996; Steefel et al., 2005; Godderis et al., 2006). However, the profile calculator addresses a common situation in which weathered regoliths are characterized in terms of element and mineral distributions with depth but for which solute data are lacking. In spite of such limitations, the discussion will demonstrate that the calculator reproduces the major profile features for the Santa Cruz terraces.

Only the weathering reactions of plagioclase (albite) and K-feldspar to kaolinite are considered in the calculations (see Appendix II).

$$\mathrm{NaAlSi_3O_8 + H^+ + 9/2H_2O \rightarrow Na^+ + 2H_4SiO_4 + 1/2Al_2Si_2O_{15}(OH)_4;} \quad \log K_{\text{plag-kaolinite}} = -2.64 \tag{9}$$

and

$$\mathrm{KAlSi_3O_8 + 9/2H_2O \rightarrow K^+ + 2H_4SiO_4 + 1/2Al_2Si_4O_2(OH)_4;} \quad \log K_{\text{Kspar-kaolinite}} = -5.30 \tag{10}$$

The mass of mineral reacted at depth z (m) and time increment t (kyrs) (see Appendix II) is defined by the expression

$$\Delta M_{z,t} = S_{z,t} \cdot t \cdot R, \tag{11}$$

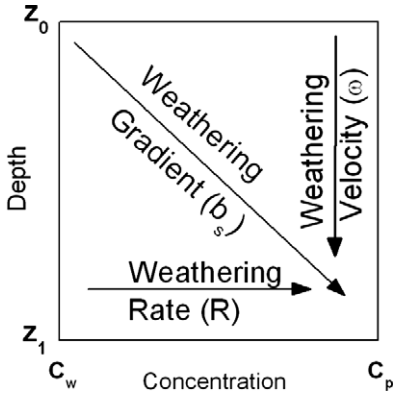

Fig. 13. Graphical representations of weathering showing the relationship between weathering rate, gradient and velocity, Eq. (7).

where $S_{z,t}$ is the volumetric surface area of this increment.

The weathering rate R is defined in terms of simplified version of rate expression Eq. (8) such that

$$R = k_r(1-\Omega)^n \tag{12}$$

Near-term-saturation effects are described by an exponential function of the saturation index Ω (Brantley, 2003). This index is the ratio of the reaction quotients to the equilibrium constants defined in Eqs. (9) and (10). These constants were taken from the most recent thermodynamic database (2005) in PHREEQEC Version 2 (Parkhurst and Appelo, 1999) and corrected to an average soil temperature measured in the Santa Cruz terraces (15 °C).

The reaction quotients, defined by Na^+, K^+ H^+ and SiO_2 concentrations (activities), are generated by the dissolution of plagioclase and K-feldspar and are fixed by their respective solubilities Eqs. (9) and (10). Aluminum is considered conservative and does not appear as a solute species. The reactions are linked by the common concentration of dissolved silica, thus requiring parallel calculations for the weathering of plagioclase and K-feldspar to kaolinite (Appendix II). The pH inputs for each terrace (5.97–6.45) were based on average field measurements. A detailed discussion of pH and other pore water solutes will be presented in a companion paper.

Aqueous concentrations are used only in determining the saturation index (Ω). The effects of specific aqueous species, such as H and Al ions, on the weathering rate Eq. (8) are not considered (Oelkers and Schott, 1995). Likewise, the simple exponential dependence of the weathering rate on the saturation index does not incorporate more complex interpretations of the role of reactions affinities on kinetic mechanisms (Burch et al., 1993; Hellmann and Tisserand, 2006).

For any depth z and time t, the ionic activity product was set equal to that of the solute concentrations. The solute concentration of a species is determined as follows (see Appendix II)

$$c_{z,t} = \frac{\beta\left(\sum_{i=1}^{z-1} M_{z,t} - \sum_{i=1}^{z-1} M_{z,t-1}\right)}{q_h \cdot (t_t - t_{t-1})}, \tag{13}$$

where β is the stoichiometric coefficient for the species in the feldspar Eqs. (9 and (10) and q_h is the hydraulic flux ($m\ s^{-1}$) which describes the rate of pore water movement through the profile. Eq. (13) defines the solute concentration at a given depth as the amount produced from feldspar reaction in the overlying regolith during the time increment between t and $t-1$ divided by the total volume of water that moved through the system. This volume is the product of the hydraulic flux and time. The Si concentration is equal to the sum of parallel calculations for both plagioclase and K-feldspar.

The initial geometric surface area of a mineral in the protolith S^o_{geo}, defined on a volumetric basis, ($m^2\ m^{-3}$), is

$$S^o_{geo} = \frac{6}{\rho d} \cdot 10^4 \cdot m_w \cdot M_p \tag{14}$$

where ρ is the mineral densities ($g\ cm^{-3}$), m_w is molar weight ($mol\ g^{-1}$), d is the average feldspar grain diameter (cm) and M_p is the initial molar concentration in a specific terrace. The volumetric feldspar surface $S_{z,t}$, in a given reaction increment, is related to the mass of residual feldspar present, i.e., $(M_i - M_{t-1,d})/M_p$ by the exponential constant α such that

$$S_{z,t} = \lambda S^o_{geo} \cdot \left(\frac{M_p - M_{z,t-1}}{M_p}\right)^{\alpha}, \tag{15}$$

where λ is the surface roughness factor described on a time-dependent basis by White and Brantley (2003).

4.3. Controls on mineral weathering

Only four variables are considered in the profile calculator; the fluid flux q_h Eq. (13) the rate constant k_r, Eq. (12), the exponential saturation index term n Eq. (12) and the exponential surface area function α Eq. (15). A simple least-square-minimization was applied between the fitted and field-based feldspar profiles using variations in only q_h and k_r, the two parameters found to have the largest impact upon the shape and position of the calculated weathering profiles. For the SCT 5 plagioclase profile (Fig. 14a–c), a least-squares minimization produced a unique pair of fitting parameters ($q_h = 0.058\ m\ yr^{-1}$ and $k_{plag} = 4.8 \times 10^{-16}\ mol\ m^{-2}\ s^{-1}$).

4.3.1. Role of fluid flow

The amount of water that moves through a terrace, i.e., the hydraulic flux q_h, was determined to be the principal control on the development of the plagioclase weathering profile and the total mass of plagioclase reacted ΔM_{plag}. The strong sensitivity of the SCT 5 plagioclase profile to flow rate is shown in Fig. 14a, in which the best fit value $q_h = 0.058\ m\ yr^{-1}$ (solid line) is arbitrarily increased and decreased by factors of 2 and 4 (dashed lines).

Slower fluxes ($q_h/2$ and $q_h/4$) produced shallower weathering profiles (lower values of b_s in Fig. 14a) because pore waters became thermodynamically saturated with plagioclase at shallower depths (Fig. 15a). Increasing the flow rates ($2q_h$ and $4q_h$), in contrast, progressively deepened the plagioclase profiles thereby increasing the

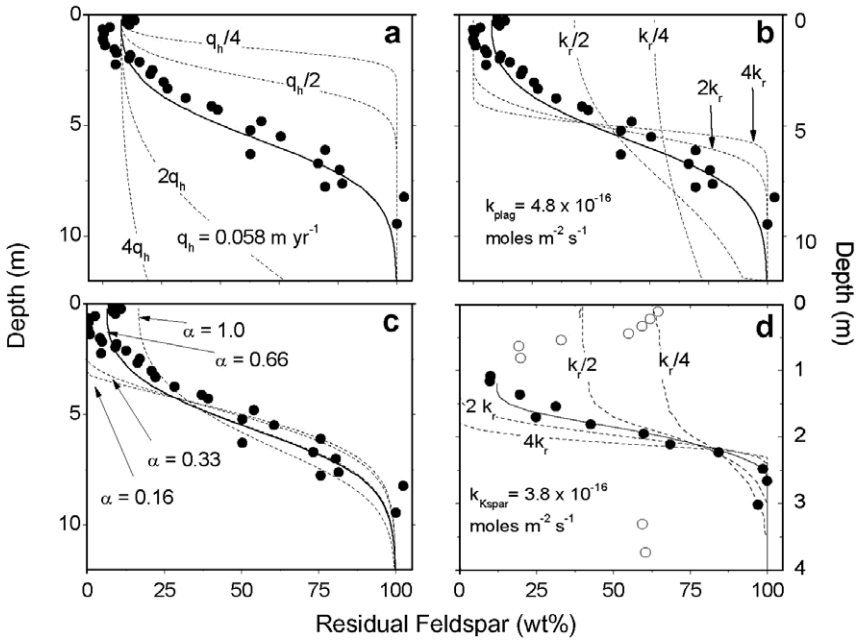

Fig. 14. Comparison between measured and calculated feldspar distributions in SCT 5. In plots (a), (b) and (c), the solid lines are the best least-squares fits to the measured plagioclase profiles (●) using a fluid flux of $q_h = 0.058\ \mathrm{m\ yr^{-1}}$ and a weathering rate constant of $k_{plag} = 4.8 \times 10^{-16}\ \mathrm{mol\ m^{-2}\ s^{-1}}$). In plot (d), the best fit to the K-feldspar profile is shown using $q_h = 0.058\ \mathrm{m\ yr^{-1}}$ and a weathering rate constant of $k_{plag} = 3.8 \times 10^{-16}\ \mathrm{mol\ m^{-2}\ s^{-1}}$. Dashed lines in each plot show the effects on calculated profiles by increasing and decreasing q_h, k_{plag} and the surface area exponential α Eqs. 9, 10 and 12. Open circles indicate data not fitted in calculation.

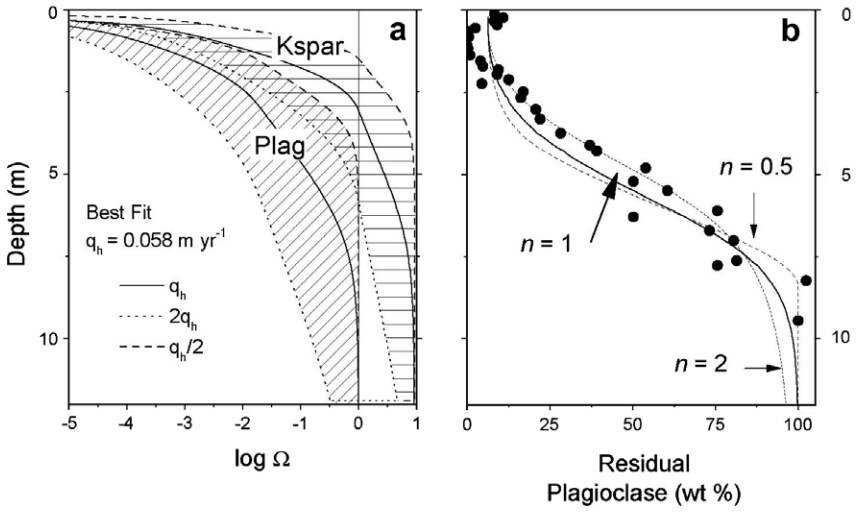

Fig. 15. Predicted effects of fluid saturation on feldspar weathering in the SCT 5 terrace profile. (a) Fluid saturation indexes for plagioclase and K-feldspar (Ω in Eq. (12) plotted as functions of terrace depth. Results are generated using both the best-fit fluid flux q_h (solid lines) and lower and higher q_h values (dashed lines). $\Omega < 0$ indicate undersaturation and $\Omega > 0$ indicate supersaturation. (b) The effect of the exponential saturation term n Eq. (12) on the shape of the plagioclase weathering profile.

depths at which plagioclase became saturated (Figs. 14a and 15a). The flow rates also largely controlled the total amount of plagioclase weathered from the SCT 5 profile. The best fit fluid flux $q_h = 0.058\ \mathrm{m\ yr^{-1}}$ resulted in a total loss of 6.8 kmol of plagioclase from weathering over 226 kyrs (ΔM_t in Eq. (6) compared a loss of 2.5 kmol for a lower flux ($q_h/4$) and 40 kmol for a higher flux ($4q_h$).

4.3.2. Role of the reaction rate constant

The SCT 5 plagioclase profile was optimally fitted using a kinetic rate constant $k_{plag} = 4.8 \times 10^{-16}\ \mathrm{mol\ m^{-2}\ s^{-1}}$ (Fig. 14b). Higher values of $2k_{plag}$ and $4k_{plag}$ produced progressively flatter, shallower gradients (lower values of b_s) with larger changes in residual plagioclase contents over smaller depth intervals. Lower values of $k_{plag}/2$ and $k_{plag}/4$ produced progressively steeper slopes (higher values of b_s)

and smaller changes in residual plagioclase with depth (Fig. 14b). These lower k_{plag} values extended weathering deeper into the SCT 5 profile by producing more dilute solutes that remained thermodynamically unsaturated with respect to plagioclase at greater depths, an effect similar to increasing the fluid flow rates (Fig. 15a).

Unlike for pore water flow, increases in the rate constant k_{plag} did not significantly affect the total amount of plagioclase reacted in the profile (ΔM in Eq. (6). Graphically, this is apparent in Fig. 14b, where increases in k_{plag} "rotate" the weathering gradient b_s upward at higher residual plagioclase concentrations, increasing the weathering intensity at shallower depth but also decreasing it at greater depths. The net result is that the amounts of plagioclase reacted underneath the different curves in Fig. 14b are about the same. The best fit rate ($k_{plag} = 4.8 \times 10^{-16}$ mol m^{-2} s^{-1}) produced a total plagioclase loss of $\Delta M = 9.8$ kmol in the profile while higher and lower values of 4 k_{plag} and $k_{plag}/4$ produce similar losses of $\Delta M = 10.2$ and 8.5 kmol, respectively. These results are contrasted against large changes in the amount of plagioclase reacted by comparable increases or decreases the fluid flow rate (Fig. 14a).

The weathering intensity is dependent principally on the depth at which pore waters reach thermodynamic saturation (Fig. 15a) which is ultimately controlled by the volume of water that moves through the regolith and not on kinetics which control how fast the plagioclase dissolves.

4.3.3. Role of surface area

The volumetric surface area of plagioclase in the protolith was first determined as a geometric equivalent S^o_{geo} based on average grain sizes measured in each terrace, feldspar abundances and regolith density Eq. (14). S^o_{geo} was then converted in Eq. (15) to the BET-based equivalent S^o using a surface roughness function λ (White and Brantley, 2003). For the 226 kyr old SCT 5 profile, $\lambda = 160$ and $S^o_v = 9.8 \times 10^4$ m^2 m^{-3} (Appendix II). The roughness factor is comparable to averages previously determined for plagioclase in the Merced chronosequence (White et al., 1996).

During subsequent weathering, the volumetric surface area decreases with declines in the residual feldspar content. The exponential term α in Eq. (15) describes how this decrease occurs which impacts on the slope of the weathering profiles shown in Fig. 14c. For shrinking spheres, the geometric relationship between surface and volume is $\Delta S_{geo} \propto \Delta V^{2/3}$, in which case, the exponential term in Eq. (15) becomes $\alpha = 0.66$. This relationship requires that the surface area decreases at a slower rate than the loss of mineral mass Eq. (15).

If the mineral grain surfaces become more pitted and etched with continued weathering, the resulting increase in surface roughness λ would further diminish the mineral surface to volume relationship Eq. (15). The overall effect of increasing roughness, as shown by declining values of $\alpha = 0.33$ and 0.16 in Fig. 14c, is to accelerate weathering at lower residual feldspar contents. This decreases the weathering gradient b_s Eq. (7) and increases the profile linearity at shallow depth (Fig. 14c). In reality, the surficial addition of eolian plagioclase and subsequent bioturbation make for imprecise determinations of the shape of the plagioclase weathering profile at shallow depths. For the present calculations, simple spherical reductions in size are assumed ($\alpha = 0.66$) with a constant surface roughness of $\lambda = 160$.

4.3.4. The role of differing feldspar solubilities

The persistence of K-feldspar compared to plagioclase is a significant weathering characteristic in the Santa Cruz Terraces (Fig. 4) as well in many natural environments (Nesbitt and Young, 1984; White et al., 2001). This difference is not replicated experimentally, where K-feldspar and plagioclase rates are similar (see reviews by Blum and Stillings, 1995; White and Brantley, 2003). This contrast is commonly attributed to the fact that experimental dissolution studies are generally conducted far from equilibrium while natural weathering generally occurs much closer to equilibrium. Such natural weathering commonly reflects differences in feldspar solubilities rather than differences in kinetic rates (White et al., 2001). Also, as implied by Eqs. (9) and (10), at near saturation, the rates of feldspar dissolution may become linked to the rates at which secondary phases such as kaolinite precipitate.

K-feldspar distributions between 1.0 and 2.6 m in the SCT 5 profile were fitted using the spreadsheet profile calculator (Fig. 14d). Samples shallower than these depths reflect eolian inputs. Variations in residual K-feldspar at greater depths are attributed to depositional differences. The computed best fit generated a K-feldspar rate constant of $k_{kspar} = 3.8 \times 10^{-16}$ mol m^{-2} s^{-1} which is only about 20% slower than for plagioclase ($k_{plag} = 4.8 \times 10^{-16)}$ mol m^{-2} s^{-1}), implying that the large difference in the respective feldspar weathering profiles (Fig. 14) are controlled by their respective solubilities and by their kinetic rates of reaction.

The respective slow rate of K-feldspar dissolution reflects its own lower solubility (about 500 times less than plagioclase in Appendix II) and the fact that the reactions of both feldspars are linked via dissolved SiO_2 Eqs. (9) and (10). The dissolution of more soluble plagioclase further promotes K-feldspar saturation via this common solute. This effect is computationally demonstrated by the fact that K-feldspar becomes progressively more supersaturated at depths below which it no longer reacts (Fig. 15a).

The coupled but distinctly different feldspar solubilities strongly influence their respective weathering profiles. As previously shown (Fig. 14b), increases in the plagioclase weathering rate k_{plag}, at a constant fluid flux q_h, flattens the weathering gradient b_s, producing more intensely weathered profiles at shallower depth. For K-feldspar, comparable increases in k_{kspar} also increase the weathering intensity at shallower depths (Fig. 14d). However, unlike for plagioclase, corresponding decreases in k_{kspar} do not extend the penetration depth of the weathering profile because K-feldspar remains thermodynamically limited by a lower solubility and the continued faster reaction of plagioclase.

4.3.5. Role of thermodynamic saturation

Experimental studies conclude that feldspar dissolution rates decrease as coexisting solutions approach thermodynamic saturation (Burch et al., 1993; Oelkers, 2001). Under

natural weathering conditions, with generally much higher rock-to-water ratios than those in experimental systems, the reaction of even very small amounts of feldspar should quickly produce near-or-saturated fluid thermodynamic conditions. This conclusion is born out by a limited number of detailed determinations of the thermodynamic states of natural ground waters and pore waters which show them to be close to feldspar saturation (Gislason and Arnorsson, 1990; White et al., 2001; White et al., 2005). In a subsequent paper, detailed analyses of pore water solutes in the Santa Cruz terraces also confirm near-saturated or saturated weathering conditions.

In the profile calculator the effect of near-saturation on the weathering rate is dependent on the value of exponential term n Eq. (12). A range of values of $n = 0.5$–2 have been used to describe the dissolution and precipitation of minerals; including feldspars (see Brantley, 2003). Larger n values ($n = 2$ in Fig. 15b) suppress plagioclase weathering at near-saturation, producing a profile that asymptotically approaches protolith compositions at greater depths (15B). Decreases in n ($n = 0.5$ in Fig. 15b) decreases the near-saturation effect and increases the linearity of the weathering profile at depth.

Delineating the exact effect of the exponential saturation term n Eq. (12) on the shape of weathering profiles is dependent on very accurate determinations of initial protolith composition and the curvature of gradients that reflect the initial phases of weathering in the deepest portions of the regolith. Even for the well-defined plagioclase SCT 5 profile, n can not be reliably estimated. For the calculations discussed in this paper, a value of unity is assumed ($n = 1$ in Fig. 15b).

While thermodynamic saturation is the major control on weathering rates, the influence of the near-saturation term is not particularly significant in determining the geometry of the weathering profile nor the amount of plagioclase reacted. For practical purposes, the weathering rates R becomes equivalent to the kinetic rate constant k_r in Eq. (12). This conclusion again emphasizes the overriding importance of solute transport on rates of chemical weathering in the Santa Cruz terraces.

4.4. Comparing terrace weathering profiles

A comparison between the measured and calculated plagioclase profiles for all the Santa Cruz terraces are shown in Fig. 16 (solid points vs. solid curves). Individual profiles were generated using the best-fit values for the fluid fluxes q_h and kinetic rate constants k_{plag} assuming constant exponents for surface area and near-saturation effects, i.e., $\alpha = 0.66$ and $n = 1$. Fluid fluxes predicted from the calculations ranged from a minimum of 0.025 m yr^{-1} for SCT 1 to a maximum of 0.12 m yr^{-1} for SCT 2. Corresponding weathering rate constants ranged from a minimum of $k_{plag} = 8.0 \times 10^{-16}$ mol m^{-2} s^{-1} for SCT 1 to a maximum of $k_{plag} = 14 \times 10^{-16}$ mol m^{-2} s^{-1} for SCT 2 (Fig. 16).

Ideally, each profile in the Santa Cruz chronosequence is a snapshot in time of how the original protolith evolved over 226 kyrs of weathering. The profile calculator permits extrapolations to what profiles looked like in the past as well as to what they will look like in the future, given present weathering conditions, i.e., constant values of q_h and k_r. For example, the dashed lines for SCT 1 plot (Fig. 16) represent a sequential forward extrapolation in time to the ages of the SCT 2 through SCT 5 profiles using the present day SCT 1 weathering parameters. Conversely, the SCT 5 plot contains profiles that are extrapolated backward in time to the ages of SCT 4 through SCT 1 profiles using present day weathering SCT 5 parameters.

If current weathering conditions remained identical for each of the five terraces, the profile geometry and the total amount of plagioclase weathered should be identical after 226 kyrs of weathering. Overall chronosequence development, represented by the shaded areas in Fig. 16, is generally similar when using the SCT 2, SCT 3, SCT 4 and SCT 5 profiles as the baselines. Clearly the greatest discrepancy occurs in the forward extrapolations in time of the SCT 1 terrace. These results predict a much less intensively weathered sequence of terraces than that which exists today. This discrepancy results primarily because the fitted fluid flux q_h, the principal parameter controlling weathering, is significantly lower for SCT 1 than for the other terraces (Fig. 16 and Table 6).

Independent estimates of present day fluid fluxes through the terraces can be made using Cl solute mass balances (Stonestrom et al., 1998)

$$q_h = q_{precip}\left(\frac{c_{Cl,precip}}{c_{Cl,porewater}}\right) \quad (16)$$

where q_{precip} is the average annual precipitation (m yr^{-1}) and $c_{Cl,precip}$ and $c_{Cl,porewater}$ (μM) are the respective average Cl concentration in precipitation and in pore waters collected in suction water samplers emplaced near the base of each terrace profile (Table 6). Details on hydrochemical techniques and solute data are described in detail in a subsequent paper.

Resulting fluid fluxes, based on Cl balances in the terraces, are generally compatible with best-fit estimates based on the spreadsheet calculations (Table 6). For example, the pore water flux through SCT 5, based on Cl Eq. (16), is only slightly faster, $q_h, = 0.088$ m yr^{-1}, than the best-fit value using the spreadsheet calculator, $q_h = 0.058$ m yr^{-1} (Fig. 14a). SCT 1 has consistently the slowest fluid fluxes for any of the terraces ($q_h = 0.057$ from Cl balances and 0.025 m yr^{-1} from the weathering calculator). These slower fluxes, at least under present conditions, reflect lower precipitation at lower elevation, in addition to higher transpiration rates associated with denser coastal vegetation.

Fluid fluxes determined from the profile calculator represent values averaged on the geologic time scale of terrace development while those determined from Cl balances reflect contemporary conditions corresponding to the residence time of the pore waters. The general agreement implies that average climatic and hydrologic conditions controlling flow fluxes has not changed significantly in the last quarter-million years at the Santa Cruz sites.

Plagioclase weathering rates for the individual Santa Cruz terraces, calculated via the profile calculator, are compared in Fig. 17 to plagioclase weathering compiled from literature (White and Brantley, 2003 along with several

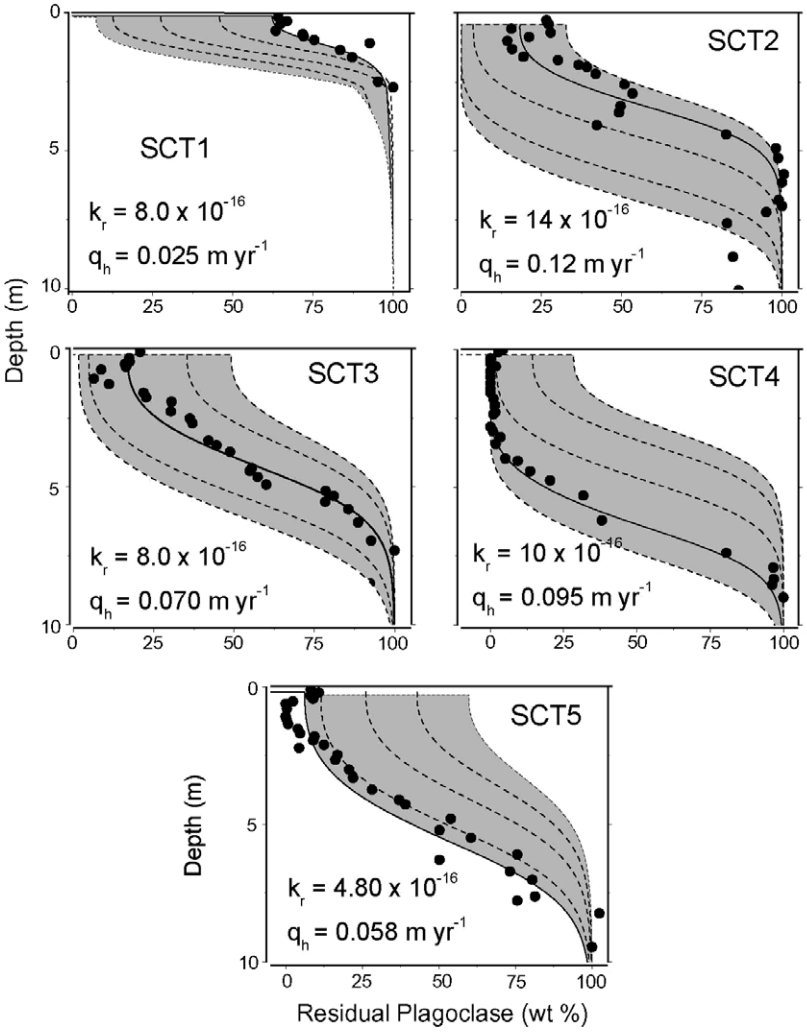

Fig. 16. Comparison of measured plagioclase distributions (solid points) with the best-fit calculated profiles (solid lines) using the indicated fluid fluxes q_h (m yr^{-1}) and rate constants k_{plag} (mol m^{-2} s^{-1}). The dashed lines correspond to the predicted weathering profiles for the other terraces based on these respective fits. Terrace profiles increase with depth in the order SCT 1 to SCT 5. The shaded area corresponds to the range in predicted weathering profiles generated for the complete chronosequence.

Table 6
Long-term fluid fluxes fitted to weathering profiles (Appendix II) compared to contemporary fluxes based on solute Cl balances Eq. (16)

	Fluid flux, q_h (myr^{-1}), profile fit	Fluid flux, q_h (m yr^{-1}), Cl balance	Average precipitaion (myr^{-1})	Average Cl precipitaion (μM)	Average Cl porewater (μM)
SCT 1	0.025	0.057	0.371	272	1170
SCT 2	0.120	0.174	0.520	254	768
SCT 3	0.070	0.127	0.613	163	583
SCT 4	0.095	0.115	0.371	140	452
SCT 5	0.058	0.088	0.586	171	1136

newer references). Where required, rates are normalized to BET surface area (λS^{o}_{geo} in Eq. (15)). In addition, no distinction is made between whether weathering rates or rate constants are reported in the literature (R vs. k_r in Eq. (12)).

Due to the relatively small age span of the Santa Cruz terraces (65–226 kyrs), plagioclase weathering rates do not decline with time as does the overall trend in the rate data shown n Fig. 17 (see discussion in White and Brantley, 2003). However the Santa Cruz rates correlate closely with those determined for comparable weathering environments. For example the weathering rate for SCT 5 ($\log k_{plag} = -15.3$ mol m^{-2} s^{-1} at 226 kyrs) is in close agreement with both contemporary and long-term rates determined by White et al. (1996, 2005) for alluvial river

terraces near Merced California ($\log k_{plag} = -15.1$ and -15.7 mol m^{-2} s^{-1} at 250 kyrs). Such close agreement attests to our increasing ability, given detailed geochemical and hydrologic data, to accurately determine natural rates of silicate weathering.

4.4.1. Steady-state versus non-steady weathering profiles

Geomorphic steady-state is commonly defined as the condition when the rate of physical erosion of a regolith surface is equal to rate of soil formation (Heimsath et al., 1997; Riebe et al., 2003). Under such conditions, weathering profiles will be spatially static or at steady state if they retreat into the protolith at the same rate as the regolith surface is denudated. With the lack of significant physical erosion (Perg et al., 2003), the Santa Cruz weathering profiles will never meet this condition but rather will continually deepen with time relative to the land surface (Fig. 16).

Steady-state profile development can be alternately defined in terms of the geometric configuration of a profile rather than on its spatial position. Under constant weathering conditions (R and q_h are invariant), a profile is geometrically at steady state when it becomes fixed by end compositions; at a shallow depth where the residual mineral is completely depleted $C_w = 0$ and at some greater depth where residual concentration reaches the protolith concentration $C_w = C_p$ (Fig. 13). In the absence of physical erosion, each point in the profile will move downward at the same velocity ω as these endpoints, preserving the overall profile geometry over time.

The geometry of the present day SCT 4 plagioclase profile (194 kyrs old) is currently at steady state (Fig. 18a). Plagioclase is essentially removed to a depth of 3 m. The sigmoid-shaped weathering profile is fixed between this point ($C_w = 0$) and a depth of about 8 m where $C_w = C_p$ (100% residual plagioclase). A forward projection in time to 300 kyrs in Fig. 18a and a backward projection to 125 kyrs produce profiles that have the identical geometry of the present day profile but are spatially transposed either downward or upward relative to land surface based on the weathering velocity ω. During this entire time, the rate at which plagioclase is lost from the profile remains constant $\Delta M/\Delta t = 75$ mol kyr^{-1}.

In contrast, the younger SCT 2 plagioclase profile (90 kyrs old) has not yet reached a steady-state geometry (Fig. 18b). Approximately 20 wt% of the residual plagioclase remains in the upper 1 m of the terrace (excluding higher surficial concentrations due to relatively recent eolian deposition). Profile concentrations increase with increasing depth, reaching the original protolith plagioclase concentration at about 6 m. Calculations backward in time (Fig. 18b) indicate that at 50 kyrs, the SCT 2 profile was fixed at shallow depths by even higher residual plagioclase (50%), resulting in a narrower concentration range in the profile and a steeper weathering gradient than what currently exists.

For the immediate future, the shape of the SCT 2 weathering profile will continue to evolve until about 160 kyrs, at which time shallow residual plagioclase will be finally depleted ($C_w = 0$). After this time, the geometry will become fixed (compare the 160 and 300 kyr profiles in Fig. 18B) and all points in the profiles will be spatially transposed downward relative to land surface at a constant weathering velocity, ω.

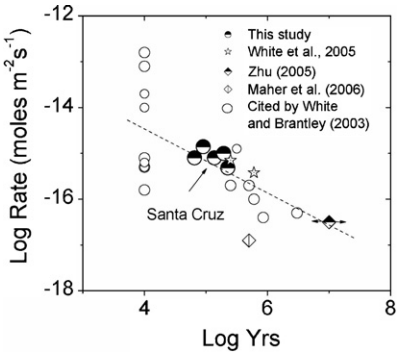

Fig. 17. Relationship between natural plagioclase weathering rates and approximate regolith ages. Data include the results of the present Santa Cruz study (see Fig. 16) and other rates reported in the literature. Rates are normalized to BET surface areas using an approach described by White and Brantley (2003). Dashed line corresponds to linear fit through data. (See above-mentioned references for further information.)

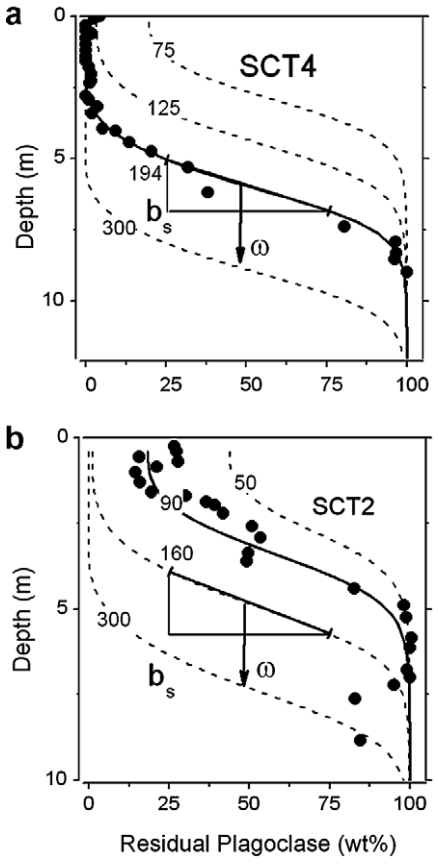

Fig. 18. Evolution of plagioclase weathering profiles in the SCT 4 and SCT 2 terraces. Measured plagioclase profiles are represented by solid circles (●), Solid lines are best fits to present day conditions and dashed lines are extrapolated profiles forward and backward in time.

Under non-steady-state conditions (0–160 kyrs) plagioclase losses in the SCT 2 terrace has decreased with time and will continue to do so into the immediate future. This results from the fact that the total amount of feldspar in the upper part of the profile that is undergoing active weathering becomes less with time. For example, at 50 kyrs (Fig. 18b) the rate of plagioclase loss $\Delta M/\Delta t = 68\ \text{mol kyr}^{-1}$, at 90 kyrs (present day), $\Delta M/\Delta t = 63\ \text{mol kyr}^{-1}$ and at the time profile geometry becomes fixed (160 kyrs) $\Delta M/\Delta t = 60\ \text{mol kyr}^{-1}$ After 160 kyrs, the weathering profile will be at steady-state and the rate of plagioclase loss constant.

Calculations indicate that both the SCT 2 and SCT 4 terraces evolve from non-steady to steady state profile geometries at comparable times, i.e., 160 and 125 kyrs respectively (Fig. 18). The difference is that steady state will be achieved in the future for the younger SCT 2 terrace while it was achieved in the past for the older SCT 4 terrace. Fig. 16 indicates that the profile geometry of the youngest SCT 1 terrace (65 kyrs old) is the least evolved and will achieve steady state only after about 225 kyrs of weathering. In contrast, SCT 3 and SCT 5 terraces are currently at or close to steady state and will remain so in the future.

For profile evolution in the presence of physical erosion, the transition between non-steady-state and steady-state profile geometries will depend on the magnitude of physical denudation D relative to the weathering velocity ω (both measured as m kyr^{-1}). Geomorphic steady-state conditions, defined as $D = \omega$, produce profiles that are also geometrically at steady-state regardless of their stage of development. For example, the non-steady-state profiles at 50 and 75 kyrs for the SCT 2 and SCT 4 terraces (Fig. 18) would become preserved indefinitely if the soil surfaces became denudated at the same rate as these profile penetrate into the protoliths, i.e., $D = \omega$. In contrast, if $D > \omega$, the profile geometry will appear to regress with time and will never reach steady state. Finally, if $D < \omega$, geometric evolution to steady state will occur at a rate dependent on the relative magnitudes of D and ω. The most rapid rate of terrace evolution occurs when $D = 0$, which is the case for the Santa Cruz terraces.

4.4.2. Simple methods for estimating weathering velocities and rates

Up to this point in the discussion, the weathering velocity ω has not been explicitly considered in profile development. Velocities can be graphically determined by measuring the difference in vertical displacements of successive profiles generated by the weathering profile calculator (vertical arrows in Fig. 18) and dividing that value by the difference in the profile ages. Such an approach results in values of $\omega = 0.040$ and $0.031\ \text{m kyr}^{-1}$ for the SCT 2 and SCT 4 plagioclase profiles. As predicted by Eq. (7), the higher weathering velocity for the SCT 2 profile produces a steeper weathering gradient than does the velocity for SCT 4 (Fig. 18).

Weathering velocities can be more rigorously determined by considering that the vertical displacement of the profiles with time is primarily controlled by the fluid flux. The dominance of q_h on the profile geometry at any given time was established by the profile calculations shown in Fig. 14a. For such saturation-limited conditions, the weathering velocity can be defined as

$$\omega = q_h \cdot \left[\frac{m_{sol}}{M_{total}}\right], \tag{17}$$

where ω proportional to q_h and the ratio of m_{sol}/M_{total} (both units are mol m^{-3}) which defines the mass of plagioclase dissolved in a thermodynamically-saturated volume of pore water Eq. (9) relative to the initial mass of plagioclase present in the protolith.

The velocity ω at which the initial point where $C_w = 0$ moves downward through the profile is governed by rate at which all the plagioclase, initially contained in the protolith M_{total} is completely dissolved by the pore water. Thus, ω equals the amount of plagioclase that can be solubilized in a given volume of water m_{sol} times the rate at which water moves through the regolith q_h. For steady-state profile geometry, every other point in the profile must also move downward at the same rate ω. For sparingly soluble plagioclase, the amount of mineral that can be dissolved in a single volume of pore water is very small compared to the amount initially present in the regolith, i.e., $m_{sol} \ll M_{total}$. Therefore, many pore volumes of water are required to completely solublize M_{total}. The consequence is that the solid-state weathering velocity is much slower than the fluid flux, i.e., $\omega \ll q_h$ (m yr^{-1}).

The respective fluid fluxes through the SCT 2 and SCT 4 terraces are 0.12 and $0.095\ \text{m yr}^{-1}$, respectively (Table 6). The mass density of plagioclase in each protolith, based on quantitative XRD analyses, is 2300 and $2360\ \text{mol m}^{-3}$, respectively. Based on the average pH and the solubility quotients in Eq. (9), the amount of plagioclase dissolved in pore water in both terraces is $0.77\ \text{mol m}^{-3}$. The resulting weathering velocities for SCT 2 and SCT 4 are $\omega = 0.040$ and $0.031\ \text{m kyr}^{-1}$ Eq. (17). These values are identical to those determined graphically from the profiles generated by the weathering calculator (Fig. 18). This similarity is expected because both approaches Eq. (17) and Appendix II describe the downward advancement of the weathering profile based on solubility-limited fluid transport.

Combining Eqs. (7) and (17) produces an expression for the weathering rate R.

$$R = \left[q_s \cdot \frac{m_{sol}}{M_{total}}\right] \cdot \left[\frac{1}{S_v \cdot b_s}\right]. \tag{18}$$

The product of the parameters contained in the first set of brackets is constant across a weathering profile and equal to the weathering velocity ω Eq. (17). In contrast, the parameters with in the second set of brackets are not constant. The weathering gradient b_s will increase with decreases in the volumetric surface area S_v which corresponds to declines in residual mineral content with decreasing depth (Fig. 14c). Further nonlinearity is introduced to the weathering gradient at high residual mineral contents by near-saturation effects Eq. (12) and Fig. 14b).

An approximate solution to Eq. (18) is achieved if the weathering gradient is estimated by linear segments of the weathering profile. For example, a linear approximation of the SCT 4 profile, between 25 and 75% residual

plagioclase, produces a weathering gradient of $b_s = 1.47\ m\ mol^{-1}\ m^{-3}$ (Fig. 18a). The mean average surface area S_v, estimated at 50% residual plagioclase, is $5.89 \times 10^5\ m^2\ m^{-3}$. Combining these values with the parameters previously used to define ω in Eq. (17), results in an estimated weathering rate for SCT 4 of $R = 1.1 \times 10^{-15}\ mol\ m^{-2}\ s^{-1}$. This rate is essentially the same as that produced by the weathering profile calculator, i.e., $R = 1.0 \times 10^{-15}\ mol\ m^{-2}\ s^{-1}$ (Fig. 16). A similar comparison can be made for a projected steady-state profile for SCT 2 at 160 kyrs. For the linear portion of profile, between 25% and 75% residual plagioclase, $R \times 1.2 \times 10^{-15}\ mol\ m^{-2}\ s^{-1}$. This value is compared to $R \times 1.4 \times 10^{-15}\ mol\ m^{-2}\ s^{-1}$ generated by the weathering profile calculator (Fig. 16).

The solutions to Eq. (18) assume a linear approximation to the weathering profiles. The spreadsheet calculation also considers the non-linear portions at low residual feldspar concentrations which reflect the effects of rapidly changing mineral surface-to-volume ratios Eq. (15) and, at high residual concentrations, the non-linear influences of thermodynamic near-saturation conditions Eq. (12). The fact that these two approaches generate similar weathering rates is attributed to the general symmetry of the sigmoid shape of the weathering profile (Fig. 14). The linear approximation underestimates residual plagioclase at shallower depths and overestimates residual plagioclase at greater depths.

The similarity in two calculations implies that influences of mineral surface area-to-volume variations and thermodynamic near-saturation influences on the weathering profiles are secondary to the magnitude of the weathering velocity which is directly proportional to the fluid flux. This relationship explains the commonly observed relationship between silicate weathering rates and parameters that correlate with fluid fluxes such as precipitation and watershed discharge (Bluth and Kump, 1994; White and Blum, 1995; Dessert et al., 2003).

While a kinetic reaction term is not contained in Eq. (18), it is implicitly present in the weathering gradient b_s. Faster kinetics produce more rapid losses of plagioclase across the profile, resulting in shallower gradients while slower kinetics produces steeper gradients (Fig. 14). This geometric expression of weathering kinetics is retained through the evolution of a profile. However once a profile becomes geometrically fixed, all points move downward at the same steady state velocity ω. The reaction rate becomes independent of the weathering gradient and reaction kinetics and fixed by the rate at which water moves downward through the profile.

5. CONCLUSIONS

The marine terrace chronosequence at Santa Cruz, spanning ages of between 65 and 226 kyrs, provides a natural laboratory in which to investigate how elemental and mineral weathering profiles develop spatially and temporally under the conditions of minimum physical erosion. Weathering profiles for Na, Ca, Sr, defined in terms of mass transfer coefficients normalized against quartz, extends to depths in excess of 8 m in the older terraces. Plagioclase weathering is non-stoichiometric, with increasing losses in the order Sr > Ca > Na. Weathering profiles for K, Rb and Ba, reflecting slower K-feldspar reaction, extends to maximum depths of 4 m. Concentration reversals occur in the upper meter of the profiles indicating eolian deposition during the last glacial maximum. Elemental fluxes for the Santa Cruz terraces fall within the range of those for other marine terraces along coastal California and Oregon.

The unique composition of a Fe-rich smectite clay in the younger terrace deposits permitted tracing its source to offshore sediments. Decreases in smectite occur with decreases in terrace depth and increases in terrace age. These trends are countered by increases in secondary kaolinite and Fe-oxides which are concentrated in strongly mottled argillic horizons at depths of about 1 m. Mass balance calculations involving Al, Fe and Mg assume that smectite was initially uniformly distributed in all the terraces at concentrations similar to those now present in the youngest profile. Results indicate that while Mg is substantially lost in the older terraces, Fe and Al are conservative, being concentrated in shallow argillic horizons. This process requires upward transport of these elements, possibly as a result from active bio-pumping by the vegetation.

The spatial and temporal developments of feldspar weathering profiles are analyzed in terms of solubilities and rates of reaction. In the broadest sense, the spatial geometry of the profiles, defined by the weathering gradient, is fixed by the ratio of the weathering velocity or the rate at which the profile moves downward into the protolith, divided by the weathering rate. Increases in velocity increase the slope or gradient of the profile while increases in weathering rates decrease the slope.

The Santa Cruz profiles exhibit sigmoidal shapes in which weathering gradients asymmetrically increase as they approach limiting residual feldspar concentrations, i.e., the complete depletion in shallow horizons and the protolith concentration at depth. A spreadsheet calculation fits the overall geometry of the weathering profile over the time frame of the chronosequence. Rates at low and high residual feldspar concentrations are reproduced using respective exponential functions describing surface area-to-volume ratios and the approach to thermodynamic saturation of the pore waters.

While the above factors, in addition to a fitted intrinsic kinetic rate constant, influence the slope and detailed geometry of the weathering profiles; the magnitude of the feldspar losses depend principally on the weathering velocity or the rate at which the profiles propagates downward into the protolith. Weathering calculations indicate that pore waters rapidly reach feldspar thermodynamic saturation at which time, the weathering velocity becomes fixed by the flux of water. This relationship explains the commonly observed correlation between weathering rates and precipitation and recharge.

Solute-transport-limited weathering has a number of important implications. The significantly greater weathering intensity of plagioclase, relative to K-feldspar, is dependent on the large difference in their respective solubilities and not on small difference between their intrinsic kinetic rate constants. Transport control defines the amount of

feldspar weathered based on functions of the pore water flux, the amount of feldspar that can be dissolved in a given volume of water and the total amount of feldspar initially present in the protolith. Long-term fluid fluxes, determined by optimum fits to the feldspar profiles, are in close agreement with contemporary fluid fluxes determined independently based on solute Cl balances.

The above approach yields plagioclase weathering rates in the Santa Cruz chronosequence that agree closely to those reported for other weathering environments of comparable climate and age. Although solid-state element and mineral concentration profiles are commonly described in soil and regolith weathering studies, the approaches developed in this paper provide methods by which these data can yield a more fundamental understanding of weathering processes.

ACKNOWLEDGMENTS

The authors thanks George Gray and the California State Park staff at Wilder Ranch and Stephanie Mills for making sampling sites available for this study. We also acknowledge co-workers at the USGS including Dan Bain, John Fitzpatrick, Jennifer Harden, Jennifer Munster and Dylan White for their assistance. We gratefully acknowledge helpful suggestions from reviews by James Drever, Yves Godderis and Jacques Schott.

Appendix I

Solid-state oxide and mineral compositions and bulk densities of the Santa Cruz chronosequence. Data breaks are approximate contacts between terrace deposits and Santa Margarita Sandstone

Depth (m)	SiO_2	$A1_2O_3$	Fe_2O_3	MgO	CaO wt%	Na_2O	K_2O	TiO_2	Zr	Sr ppm	Rb	Ba	Density g cm^{-3}	Qtz	K-spar	Plag	Fe-oxid wt%	Illite mica	Kao-linite	Smec-tite
Ben Lomond Granite[a,b]																				
	63.6	16.96	5.03	7.93	5.74	3.34	1.68	0.66	405	—	—	—	—	30.5	7.4	52.0	—	—	—	—
Average Wilder Beach (present day)																				
Ave.	80.5	8.02	2.82	0.94	2.62	1.75	1.41	0.77	637	211	38	419	—	—	—	—	—	—	—	—
Smectite																				
Purisima	48.9	20.7	14.8	1.67	0.48	0.89	0.45	0.62						24.1	7.6	35.6	1.3	12.0	1.6	15.8
SCT 2	48.9	25.4	10.6	1.26	0.5	0.10	0.59	0.93	—	—	—	—	—	—	—	—	—	—	—	—
SCT 1 Age = 65 kyrs; Site location Lat = N 36.95411°; . Long = W 122.02651°; Elev. = 6m																				
0.15	81.5	9.63	2.34	0.51	1.50	2.16	1.85	0.45	301	189	52	547	1.13	59.2	11.9	25.2	0.4	6.9	0.0	2.8
0.30	81.8	9.60	2.30	0.46	1.38	2.07	1.87	0.44	275	190	50	514	1.59	59.5	11.6	26.3	0.4	6.6	3.7	2.1
0.40	82.1	9.36	2.20	0.44	1.40	2.08	1.85	0.47	303	175	50	540	1.75	56.2	12.3	25.5	0.4	3.1	4.7	3.0
0.65	74.9	14.26	4.36	0.78	1.48	2.26	1.37	0.53	160	189	41	393	1.79	40.8	7.5	24.9	0.3	10.3	7.9	9.8
0.77	74.2	14.26	4.75	0.91	1.61	2.41	1.35	0.48	134	212	41	448	1.86	38.0	5.1	28.2	0.4	17.0	7.1	11.1
0.85	75.0	13.49	4.60	0.91	1.66	2.43	1.43	0.42	119	212	44	432	1.77	39.8	6.7	28.3	0.3	12.9	3.2	13.8
0.98	73.8	13.75	4.97	1.10	1.94	2.60	1.40	0.38	72	241	40	620	1.61	36.6	5.6	29.6	0.2	11.6	2.2	12.2
1.10	74.5	13.61	4.25	1.08	1.92	2.74	1.46	0.37	83	247	42	540	1.67	38.1	4.5	36.4	0.3	8.4	2.0	11.0
1.35	73.8	14.66	4.06	1.08	1.70	2.65	1.61	0.36	60	234	46	527	1.63	36.9	5.9	32.8	0.2	12.5	7.8	7.8
1.61	75.8	12.89	3.57	1.06	2.05	2.73	1.49	0.36	76	246	41	492	1.65	42.6	5.8	34.3	0.3	7.6	2.6	8.7
2.50	75.6	12.61	3.20	1.18	2.21	2.96	1.81	0.32	74	275	50	564	1.74	42.0	7.5	37.4	0.4	4.9	1.9	7.5
2.70	75.2	12.93	3.26	1.18	2.14	2.95	1.93	0.31	69	299	62	667	1.71	42.1	9.9	39.3	0.0	9.1	1.5	1.5
SCT 2 Age = 90 kyrs; Site location Lat = N 36.967968°; Long = W 122.085047°; Elev. = 67m																				
0.25	79.6	9.43	6.03	0.36	0.67	1.07	2.22	0.49	278	109	75	595	1.13	64.3	16.3	10.3	1.0	6.7	10.5	3.8
0.40	80.6	9.57	5.00	0.38	0.64	1.11	2.14	0.49	281	106	73	583	1.59	62.2	16.8	10.5	1.1	2.9	5.1	3.4
0.56	80.0	9.98	5.45	0.35	0.53	1.04	2.14	0.50	269	101	70	549	1.75	67.1	15.3	6.1	1.0	5.8	5.0	0.8
0.70	79.6	11.27	4.76	0.36	0.49	0.98	2.02	0.51	249	94	64	516	1.79	58.9	14.1	10.8	1.2	6.4	7.7	2.0
0.86	76.6	13.60	6.01	0.40	0.35	0.74	1.76	0.55	211	75	64	470	1.86	55.2	14.2	8.2	1.7	9.3	10.9	2.6
1.00	77.9	14.29	3.65	0.45	0.37	0.86	1.84	0.57	226	83	61	469	1.77	50.1	11.5	5.6	3.2	15.8	17.1	2.9
1.30	74.4	17.85	3.81	0.57	0.32	0.79	1.59	0.64	165	75	61	397	1.61	40.5	9.4	6.1	1.6	13.8	24.6	6.1
1.58	74.9	16.73	4.01	0.59	0.39	0.96	1.85	0.56	149	89	64	419	1.67	39.3	10.1	7.5	1.4	12.9	19.5	4.1
1.70	76.9	14.54	3.39	0.72	0.52	1.28	2.17	0.48	153	118	80	524	1.63	—	—	—	—	—	—	—
1.87	76.7	14.61	3.31	0.73	0.53	1.37	2.27	0.43	124	119	79	520	1.65	43.9	11.6	14.1	0.5	8.8	13.7	10.8
1.95	76.8	14.57	3.18	0.69	0.63	1.49	2.23	0.37	95	126	75	520	1.66	42.6	11.9	15.2	0.6	8.3	16.0	8.3
2.20	76.1	14.91	3.37	0.73	0.68	1.66	2.18	0.35	74	137	70	515	1.74	41.8	11.4	16.2	0.5	9.1	15.7	10.0

2.58	73.1	16.55	4.43	0.97	0.73	1.79	2.00	0.44	70	136	66	486	1.71	—	—	—	—	—	—	—
2.91	73.8	15.79	4.13	0.92	0.82	1.99	2.12	0.41	69	147	68	518	1.66	35.0	9.9	20.6	0.6		11.9	11.8
3.37	73.6	15.71	4.34	1.04	0.83	1.97	2.09	0.43	68	155	70	525	1.63	33.7	10.0	19.2	0.4	8.9	12.8	12.3
3.60	73.5	15.93	4.42	0.92	0.83	1.95	2.02	0.43	74	151	71	503	1.72	33.7	9.5	19.0	0.6	10.2	12.9	13.0
4.06	69.0	16.80	7.06	1.67	0.68	1.75	2.09	0.86	137	127	83	497	1.70	26.8	7.4	16.4	0.8	15.1	16.3	17.7
4.40	77.6	14.01	1.12	0.34	1.48	2.30	2.99	0.18	60	218	95	712	1.60	42.7	15.6	31.9	0.2	2.3	7.4	3.8
4.90	76.8	14.34	0.98	0.29	1.83	2.60	2.95	0.21	75	240	93	665	1.46	42.0	13.9	37.9	0.1	2.6	8.6	3.8
5.26	77.2	13.97	0.78	0.23	1.81	2.67	3.11	0.15	61	253	94	779	1.52	44.3	16.2	38.2	0.1	2.0	9.3	4.1
5.84	76.7	14.06	1.15	0.29	1.88	2.65	3.03	0.20	71	258	100	782	1.52	44.9	14.9	38.9	0.1	2.2	4.4	5.5
6.14	76.9	14.00	1.15	0.28	1.88	2.69	2.90	0.19	65	257	89	692	1.48	43.2	13.3	38.7	0.2	3.8	6.1	2.2
6.78	77.7	13.55	0.83	0.25	1.80	2.59	3.04	0.17	105	276	95	867	1.6*	45.3	14.4	38.3	0.1	2.1	2.3	3.8
7.00	77.5	13.71	0.87	0.24	1.80	2.65	3.03	0.20	75	261	96	723	1.6*	44.6	14.4	38.6	0.0	3.3	4.4	2.3
7.22	77.3	13.68	1.05	0.25	1.79	2.67	3.07	0.17	60	252	104	724	1.6*	41.6	15.6	36.7	0.2	1.7	7.8	3.5
7.62	78.2	13.42	0.69	0.13	1.82	2.59	2.99	0.16	55	291	107	770	1.6*	—	—	—	—	—	—	—
8.84	78.0	13.30	0.74	0.19	1.92	2.64	3.07	0.16	58	296	101	857	1.6*	—	—	—	—	—	—	—
10.06	77.8	13.36	0.80	0.20	1.91	2.68	3.12	0.16	65	302	105	830	1.6*	—	—	—	—	—	—	—
11.28	78.9	12.93	0.57	0.07	1.83	2.60	2.97	0.13	59	307	101	813	1.6*	—	—	—	—	—	—	—
12.50	78.1	13.30	0.74	0.17	1.82	2.62	3.11	0.15	62	313	107	944	1.6*	—	—	—	—	—	—	—
13.26	77.2	13.75	1.05	0.17	1.89	2.68	3.04	0.20	72	321	106	828	1.6*	—	—	—	—	—	—	—
14.33	76.9	13.83	1.16	0.22	1.90	2.68	3.08	0.20	73	318	107	845	1.6*	—	—	—	—	—	—	—
15.34	76.0	14.32	1.20	0.32	1.92	2.72	3.20	0.24	71	319	110	822	1.6*	—	—	—	—	—	—	—
SCT 3 Age = 137 kyrs Site location Lat = N 36.976366°; Long = W 122.077621°; Elev. = 110 m																				
0.10	83.4	8.34	6.25	0.35	0.47	0.76	1.89	0.67	414	108	72	669	1.13	66.7	16.1	6.4	1.0	3.7	4.7	4.3
0.33	83.6	8.62	9.05	0.34	0.41	0.76	1.92	0.69	380	103	83	683	1.59	66.5	16.2	5.4	1.1	6.6	13.9	0.1
0.45	83.7	8.85	5.97	0.34	0.39	0.74	1.74	0.68	414	99	75	642	1.75	65.7	15.9	5.4	1.3	6.5	12.2	0.2
0.54	84.0	8.67	3.97	0.34	0.36	0.73	1.77	0.68	383	102	75	656	1.79	66.9	16.1	5.0	1.4	5.9	9.0	0.0
0.64	85.4	9.26	2.98	0.35	0.33	0.71	1.84	0.69	391	99	75	629	1.86	67.8	14.6	5.1	1.1	8.0	11.5	1.5
0.74	85.5	11.01	3.41	0.39	0.24	0.53	1.58	0.70	314	80	66	564	1.77	63.1	13.0	2.7	1.9	10.6	13.9	0.0
1.07	80.7	16.31	4.84	0.45	0.13	0.41	1.13	0.68	230	60	53	436	1.61	54.4	8.7	2.0	2.8	14.9	26.2	2.6
1.27	82.8	14.61	3.57	0.40	0.16	0.49	0.95	0.59	237	73	42	473	1.67	58.4	8.8	3.4	2.1	10.9	23.4	0.0
1.59	83.9	12.56	3.34	0.44	0.26	0.84	1.38	0.55	215	87	53	487	1.65	61.0	9.4	6.7	1.8	9.3	17.7	2.1
1.75	79.7	12.78	3.60	0.48	0.26	0.92	1.62	0.54	219	95	65	576	1.66	54.7	10.0	7.0	1.2	8.6	20.1	3.1
1.91	82.9	10.70	2.33	0.43	0.30	1.04	1.77	0.50	199	107	63	591	1.74	64.4	12.5	9.5	0.7	6.1	12.3	4.2
2.26	79.3	13.12	3.27	0.53	0.32	1.10	1.76	0.51	198	111	67	623	1.71	54.4	11.7	9.4	1.1	9.4	18.7	5.7
2.52	78.3	13.55	3.71	0.55	0.35	1.21	1.76	0.49	147	116	73	633	1.66	53.5	10.7	11.2	1.2	7.5	10.3	6.9
2.69	78.2	13.59	3.76	0.59	0.37	1.26	1.74	0.45	135	116	75	623	1.63	49.1	10.5	11.5	1.5	9.8	15.8	3.3
3.32	79.0	13.29	3.39	0.60	0.42	1.36	1.51	0.39	89	130	62	651	1.70	50.7	10.1	13.0	1.0	8.9	15.8	5.0
3.49	76.9	14.47	4.00	0.64	0.43	1.43	1.64	0.39	78	124	64	602	1.60	46.4	9.0	13.8	1.0	9.5	17.6	7.1
3.73	77.8	14.08	3.48	0.56	0.48	1.55	1.66	0.38	79	132	63	599	1.46	48.9	9.4	15.1	1.2	9.4	17.1	6.3
4.32	76.7	14.29	3.98	0.66	0.57	1.71	1.65	0.41	85	148	67	619	1.52	45.8	8.9	17.2	1.2	9.4	12.1	7.2

(*continued on next page*)

Appendix I (*continued*)

Depth (m)	SiO_2	$A1_2O_3$	Fe_2O_3	MgO	CaO wt%	Na_2O	K_2O	TiO_2	Zr	Sr ppm	Rb	Ba	Density g cm^{-3}	Qtz	K-spar	Plag	Fe-oxid wt%	Illite mica	Kao-linite	Smec-tite
4.42	78.3	13.69	3.23	0.56	0.53	1.62	1.66	0.35	76	142	67	608	1.52	—	—	—	—	—	—	—
4.64	73.6	16.26	5.07	0.71	0.60	1.67	1.55	0.44	86	143	57	633	1.48	—	—	—	—	—	—	—
4.92	76.7	14.55	3.10	0.57	0.94	1.72	2.07	0.28	114	197	68	920	1.60	—	—	—	—	—	—	—
5.15	75.6	13.40	1.80	0.37	1.00	2.04	3.24	0.34	191	191	96	747	1.6*	44.1	21.6	24.3	0.5	5.6	10.3	4.2
5.33	75.8	13.10	2.00	0.40	1.00	2.09	3.24	0.34	187	190	94	711	1.6*	43.8	21.1	25.1	0.6	5.2	3.9	4.1
5.54	75.5	13.30	1.82	0.39	1.03	2.12	3.26	0.35	197	197	94	778	1.6*	42.0	19.9	24.3	0.3	7.4	8.8	3.3
5.81	76.1	13.50	1.31	0.41	1.11	2.21		0.35	193	209	97	750	1.6*	43.2	21.2	26.5	0.3	5.9	11.3	2.5
6.29	75.2	13.40	1.77	0.42	1.16	2.24	3.31	0.37	183	219	97	853	1.6*	41.0	19.3	27.5	0.4	8.1	8.2	2.4
6.96	75.3	13.30	1.26	0.47	1.56	2.26	3.12	0.39	176	217	97	769	1.6*	41.9	19.2	28.8	0.2	6.1	6.5	2.9
7.31	74.3	14.00	1.71	0.48	1.28	2.37	3.15	0.40	180	221	93	770	1.6*	42.3	18.6	31.0	0.3	6.8	5.8	4.4
8.51	74.4	12.92	2.15	0.31	1.39	2.37	3.26	0.36	182	312	105	1210	1.6*	—	—	—	—	—	—	—
10.33	78.2	11.29	1.65	0.06	1.34	2.18	3.06	0.22	156	346	91	1400	1.6*	—	—	—	—	—	—	—
10.54	76.4	12.19	2.08	0.16	1.41	2.36	3.19	0.24	161	317	109	1130	1.6*	—	—	—	—	—	—	—
11.52	78.9	10.95	1.78	0.11	1.31	2.23	3.21	0.17	163	314	94	1080	1.6*	—	—	—	—	—	—	—
SCT 4 Age = 193 kyrs; Site location Lat = N 36.983609°; Long = W 122.077006°; Elev. = 159 m																				
0.01	84.7	6.18	5.23	0.43	0.28	0.32	1.63	1.22	1036	83	69	626	1.40	83.1	18.5	1.7	3.6	6.7	4.0	1.2
0.09	85.9	6.42	3.71	0.41	0.22	0.34	1.73	1.21	1092	77	72	605	1.54	71.4	14.5	1.1	2.9	9.9	5.8	0.0
0.33	78.2	12.59	5.40	0.47	0.22	0.29	1.57	1.23	932	69	77	542	1.61	56.0	11.3	0.0	2.8	13.7	10.9	0.0
0.50	64.4	24.50	8.16	0.51	0.12	0.13	1.01	1.11	553	42	59	374	1.48	53.5	11.5	0.7	2.2	11.3	17.0	0.0
0.61	71.1	19.29	6.72	0.44	0.03	0.13	1.15	1.08	563	41	51	414	1.41	42.0	6.6	0.0	2.3	12.9	32.0	0.8
0.79	70.0	20.51	6.89	0.42	0.03	0.12	0.97	1.03	560	38	45	344	1.31	38.1	6.1	0.0	2.1	14.2	36.0	2.7
0.99	76.1	15.94	5.34	0.35	0.02	0.16	1.28	0.77	458	46	49	441	1.31	50.6	8.3	0.0	2.2	7.8	21.2	2.0
1.21	77.4	15.71	4.58	0.31	0.02	0.17	1.30	0.48	201	47	54	449	1.32	—	—	—	—	—	—	—
1.42	77.4	16.58	3.79	0.34	0.03	0.20	1.23	0.42	138	49	49	503	1.46	47.6	8.7	0.0	0.9	10.8	28.0	3.0
1.57	76.2	17.63	3.61	0.34	0.03	0.22	1.60	0.36	95	51	59	486	1.50	44.1	10.6	0.0	0.2	9.8	30.2	4.5
1.78	75.4	18.13	3.84	0.33	0.04	0.26	1.64	0.38	107	57	63	577	1.33	45.6	10.9	0.4	0.3	11.4	32.4	5.4
2.02	77.3	16.42	3.07	0.37	0.05	0.32	2.11	0.35	119	69	76	630	1.55	49.9	15.0	0.6	0.1	9.5	24.4	5.5
2.28	78.1	15.85	2.73	0.36	0.05	0.32	2.29	0.33	116	73	71	705	1.56	47.9	16.9	0.6	0.8	5.8	19.8	6.5
2.35	77.1	16.64	3.03	0.34	0.05	0.32	2.18	0.35	107	71	69	683	1.56	45.7	15.6	0.4	0.4	8.1	25.5	5.9
2.80	79.5	14.55	2.28	0.37	0.05	0.29	2.62	0.32	150	81	86	797	1.56	48.2	19.5	0.0	0.1	8.4	20.8	5.3
2.95	79.8	13.94	2.25	0.40	0.06	0.40	2.86	0.33	138	86	98	847	1.53	49.6	21.6	0.3	0.0	10.9	17.4	2.1
3.18	77.6	15.55	3.06	0.32	0.07	0.42	2.74	0.27	110	86	85	840	1.49	—	—	—	—	—	—	—
3.43	77.9	15.87	2.44	0.50	0.09	0.39	2.34	0.50	293	76	86	761	1.42	50.2	15.5	1.4	0.0	7.3	20.0	7.3
3.96	76.9	16.44	2.53	0.63	0.13	0.43	2.38	0.55	315	79	84	741	1.33	41.9	15.8	2.0	0.2	8.7	25.3	11.5
4.04	75.5	16.87	3.18	0.67	0.15	0.51	2.50	0.60	344	83	96	744	1.41	45.9	15.9	3.7	0.4	9.3	21.6	10.6
4.42	76.4	15.60	2.96	0.65	0.20	0.68	2.81	0.63	396	136	106	1000	1.37	43.7	14.7	5.3	0.0	7.5	18.3	9.9
4.75	74.4	16.74	3.29	0.78	0.28	0.82	2.88	0.74	440	150	106	1020	1.40	40.7	13.8	8.0	0.0	12.8	17.3	10.2

5.75	79.8	13.20	1.54	0.38	0.56	1.21	2.83	0.36	202	152	80	830	1.6*	48.8	16.3	12.4	0.3	5.7	12.1	5.0
6.75	78.6	13.78	1.76	0.42	0.67	1.33	2.86	0.42	234	168	93	837	1.6*	47.1	15.7	14.9	0.0	5.2	9.8	6.0
7.75	76.8	14.01	1.70	0.41	1.64	2.31	2.65	0.44	230	257	87	838	1.6*	42.0	11.7	31.5	0.0	3.8	7.1	7.5
SCT 5 Age = 226 kyrs; Site location Lat = N 36.99466°; Long = W 122.133071°; Elev. = 190 m																				
0.11	82.8	7.28	6.63	0.33	0.44	0.46	1.35	0.62	332	72	51	455	0.95	67.6	11.1	2.6	2.6	5.1	6.1	1.1
0.22	81.3	8.10	7.38	0.35	0.38	0.45	1.33	0.64	370	70	54	462	1.17	68.5	10.7	3.4	1.8	7.3	9.0	2.8
0.33	81.4	8.97	6.42	0.38	0.36	0.45	1.35	0.66	373	67	57	466	1.40	63.7	10.2	2.6	1.6	6.8	10.6	3.0
0.44	83.3	9.98	7.26	0.35	0.32	0.42	1.32	0.68	345	65	54	458	1.45	66.0	9.5	2.8	0.9	6.3	9.2	1.3
0.54	71.3	17.53	8.56	0.42	0.26	0.23	0.87	0.76	252	43	44	322	1.22	44.4	5.7	0.8	1.2	14.6	27.4	0.0
0.63	68.3	20.17	9.40	0.44	0.21	0.11	0.56	0.75	197	33	36	262	1.40	37.3	3.3	0.0	1.1	15.3	26.0	2.8
0.81	68.1	20.02	9.77	0.47	0.12	0.13	0.53	0.77	181	32	30	247	1.48	39.5	3.4	0.1	0.6	14.5	29.1	0.0
1.08	67.9	22.30	7.85	0.50	0.07	0.09	0.45	0.81	179	25	29	190	1.42	35.3	1.7	0.0	1.2	17.0	35.5	3.2
1.16	69.2	21.88	7.10	0.46	0.07	0.10	0.42	0.77	194	23	31	202	1.42	36.3	1.7	0.1	0.6	19.8	28.5	1.9
1.36	72.4	19.55	6.11	0.43	0.07	0.13	0.52	0.73	197	27	37	201	1.42	42.3	3.4	0.3	0.5	19.5	28.3	1.5
1.54	82.2	12.20	3.63	0.34	0.07	0.20	0.77	0.58	467	39	34	302	1.61	61.3	5.4	1.3	0.4	13.7	16.3	0.2
1.70	75.6	18.44	3.81	0.42	0.11	0.25	0.66	0.71	192	41	35	263	1.48	49.4	4.3	1.5	0.6	15.4	27.0	4.0
1.81	82.6	11.46	3.40	0.33	0.15	0.44	1.11	0.50	246	58	48	386	1.35	63.2	7.3	3.0	0.4	9.0	17.8	2.7
1.95	83.1	11.20	2.89	0.31	0.16	0.49	1.39	0.46	232	70	45	453	1.41	58.4	10.3	2.8	0.5	8.6	19.1	2.1
2.11	83.5	10.93	2.53	0.31	0.18	0.57	1.56	0.44	233	75	59	510	1.53	60.5	11.8	4.0	0.2	9.3	17.5	1.5
2.23	83.1	10.85	2.70	0.30	0.20	0.61	1.77	0.46	274	83	64	570	1.53	—	—	—	—	—	—	—
2.48	83.1	11.09	2.25	0.28	0.21	0.65	1.99	0.42	205	89	62	602	1.72	58.5	14.5	5.4	0.3	6.3	16.2	4.2
2.66	83.0	10.58	2.52	0.28	0.22	0.72	2.27	0.39	222	100	70	686	1.69	56.1	17.0	5.1	0.5	9.7	9.6	0.6
3.02	83.1	10.64	2.13	0.27	0.23	0.77	2.57	0.31	160	107	80	745	1.71	59.0	17.3	6.6	0.6	4.6	8.0	4.7
3.31	82.0	12.12	2.01	0.27	0.32	0.84	2.17	0.31	135	121	71	714	1.63	55.2	16.7	7.0	0.5	10.0	12.6	1.2
3.74	76.2	15.38	4.63	0.38	0.43	0.99	1.65	0.36	87	118	59	567	1.57	43.6	10.2	8.9	0.4	10.0	19.7	6.4
4.11	79.7	14.11	2.32	0.31	0.48	1.08	1.64	0.34	102	127	62	553	1.55	48.6	10.4	11.7	0.3	7.9	20.0	5.4
4.28	81.4	12.22	1.92	0.37	0.51	1.21	2.08	0.32	305	142	75	654	1.67	55.2	13.6	12.4	0.1	5.9	11.0	5.9
4.80	77.5	15.84	1.71	0.35	0.74	1.63	1.79	0.38	86	173	68	621	1.60	—	—	—	—	—	—	—
5.21	82.3	10.94	2.13	0.37	0.71	1.51	1.80	0.24	71	171	63	638	1.82	56.7	11.7	15.9	0.4	5.0	7.7	4.4
5.49	76.5	12.67	2.71	0.42	0.82	1.76	2.17	0.28	713	203	73	713	1.51	—	—	—	—	—	—	—
6.10	74.7	13.01	3.53	0.70	1.04	2.07	1.81	0.38	637	212	63	637	1.6*	—	—	—	—	—	—	—
6.29	74.5	13.20	3.34	0.79	0.98	2.08	1.66	0.35	87	214	63	684	1.6*	56.7	11.7	15.9	0.4	4.9	7.4	4.5
6.71	74.8	12.79	3.17	0.62	1.05	2.02	1.90	0.36	724	214	68	724	1.6*	—	—	—	—	—	—	—
7.01	74.8	12.90	3.35	0.70	1.13	2.17	1.74	0.37	635	220	61	635	1.6*	—	—	—	—	—	—	—
7.62	74.3	13.23	3.38	0.73	1.10	2.19	1.80	0.36	651	225	65	651	1.6*	—	—	—	—	—	—	—
7.77	74.2	13.10	3.69	0.76	1.12	2.07	1.70	0.43	603	209	61	603	1.6*	—	—	—	—	—	—	—
8.23	77.1	13.28	0.80	0.18	1.81	2.62	2.99	0.17	850	300	103	850	1.6*	—	—	—	—	—	—	—
9.45	76.6	13.37	0.82	0.16	1.79	2.57	3.02	0.19	868	297	108	868	1.6*	—	—	—	—	—	—	—

[a] KistLer and Campion, 2001.
[b] Other reported minerals in the Ben Lomand Granite are hornblende (3.7 wt%) and biotite (12.4 wt%), data from Leo, 1965).
[*] Assumed bulk density.

Appendix II

A weatheirng profile calculator. Partial reproduction of the calcuations used to fit the plagioclase weatheirng profile in the SCT 5 terrace (see notes below for additions descriptions)

			Mineral Distributions				Surface Area					
Density		Initial	Wt%	moles	Moles	Partcle	Roughness ca	Surface	mole	m2 per	m2	
Density		conc.	mineral	/m3	interval	Size (cm)	factor	area m2/g	wt (g)	mole	interval	
1.60	(g/cm3)	Plag=	31.70	1907	191	0.019	160	1.93832	265.91	515	98311	
1600	(kg/m3)	K-spar=	17.25	994	99	0.019	160	1.93832	277.60	538	53509	
	Depth (m)	Time (s)	Time (yrs)	Solubility Product				Solute pH	Reaction			
Total	9.45	7.13E+12	2.26E+05	Plag =	-2.637			6.00	order			
Interval	0.10	7.54E+10	2.39E+03	K-spar =	-5.308			S/V	n			
Reaction Rate		moles/m2/s	moles/m2/yr	Fluid				power	1.00			
Plagioclase =		4.80E-16	1.73E-08	Conductivity	m/yr		0.050	function				
K-feldspar =		3.86E-16	1.73E-08	Volumne of water per time step (L)			1.20E+05	0.660				

	Time(j)												
Depth (i)	0	2392	4783	7175	9566	11958	14349	16741	19132	21524	23915	26307	28698
0.10	0.010	0.010	0.020	0.030	0.040	0.050	0.060	0.070	0.080	0.090	0.100	0.110	0.120
0.20	0.010	3.584	7.113	10.598	14.040	17.438	20.793	24.104	27.373	30.600	33.784	36.926	40.027
0.30	0.010	3.583	7.113	10.598	14.039	17.437	20.791	24.103	27.371	30.598	33.782	36.924	40.025
0.40	0.010	3.582	7.109	10.592	14.032	17.428	20.782	24.092	27.360	30.585	33.768	36.909	40.009
0.50	0.010	3.577	7.100	10.579	14.015	17.407	20.757	24.064	27.328	30.551	33.731	36.870	39.968
0.60	0.010	3.569	7.084	10.555	13.984	17.370	20.714	24.015	27.274	30.491	33.667	36.801	39.895
0.70	0.010	3.557	7.062	10.523	13.943	17.320	20.655	23.948	27.199	30.409	33.578	36.706	39.794
0.80	0.010	3.542	7.033	10.481	13.887	17.253	20.576	23.859	27.101	30.302	33.462	36.582	39.662
0.90	0.010	3.523	6.994	10.425	13.815	17.165	20.474	23.743	26.972	30.160	33.310	36.419	39.490
1.00	0.010	3.498	6.946	10.354	13.724	17.053	20.344	23.596	26.808	29.982	33.117	36.214	39.272
1.10											32.880	35.960	39.003
1.20											32.595	35.655	38.680
1.30											32.258	35.296	38.299
1.40											31.868	34.878	37.856
1.50											31.422	34.401	37.350
1.60											30.919	33.862	36.778
1.70											30.357	33.261	36.140
1.80											29.739	32.598	35.435
1.90											29.064	31.874	34.665
2.00											28.335	31.091	33.831
2.10											27.554	30.251	32.936
2.20	0.010	2.700	5.387	8.072	10.753	13.430	16.103	18.769	21.428	24.080	26.724	29.359	31.984
2.30	0.010	2.596	5.183	7.771	10.360	12.948	15.534	18.119	20.700	23.278	25.851	28.418	**30.979**
12.00	0.001	0.010	0.010	0.010	0.010	0.010	0.010	0.010	0.010	0.010	0.010	0.010	0.010

```
=IF($M$5*(((($F$12-M51)/$F$12)^$H$9)
*$F$20*$M$9+M51>$F$12,$F$12,IF($H$12+LOG(SUM(N$29:N50)/$M$16-
SUM(M$29:M50)/$M$16)+2*LOG((2*(SUM(N$29:N50)+SUM(N$151:N172)-SUM(M$151:M172)-
SUM(M$29:M50))/$M$16))>$H$15,M51,$M$5*(((($F$12-M51)/$F$12)^$H$9)*$F$20*($M$9*((1-
(10^(($H$12+LOG(SUM(N$29:N50)/$M$16-
SUM(M$29:M50)/$M$16)+2*LOG((2*(SUM(N$29:N50)+SUM(N$151:N172)-SUM(M$151:M172)-
SUM(M$29:M50))/$M$16)))))/10^$H$15))^$M$11)+M51))
```

The input parameters to the weathering profile calculator, used to fit the SCT 5 plagioclase and K-feldspar weathering profiles, (Fig. 14) are reproduced in the upper block of cells. The lower block of cells contains the masses plagioclase weathered (moles) arrayed in terms of increments of total time (226 kyrs) and depth (12 m). For illustrative purposes, only the initial portion and final values of the array are included. The plagioclase mass M (moles), reacted over a specific time t and t-1 and depth d and d-1 intervals, is calculated using branching *IF* statements which consider input parameters, values of preceding cells, and solubility and kinetic rate expressions. An example of the calculation shows that in the cell 30.979 moles of plagioclase are reacted between t =26,307 and 28,698 years over a depth interval of d =2.20 to 2.30 m using the formula shown in the text insert in Table 1. The first IF statement in this calculation limits the reacted plagioclase to the amount initially contained in the protolith M_p. The second IF statement stops the reaction if thermodynamic saturation is achieved.

The total amount of solute Na, K and Si within a reaction increment at time t is determined by the difference in the sums of the amount of feldspar reacted at in the overlying cells (d= from 0 to d-1) at t and that previously reacted in the same cells at t-1. Dividing this mass by the total fluid volume that was moved through the profile between t and t-1 permits converting Na, K and Si masses into concentrations. This fluid volume is calculated as the product of the fluid flux q and the time step between t and t-1 (Table 6). The calculation does not consider external solute compositions except for pH. If solute limitations are not exceed, the formula calculates the feldspar mass reacted in the cell based on the surface area $S_{d,t}$, the intrinsic rate constant k_r and a function describing the saturation state (Eqns 12 - 14). Residual plagioclase and K-feldspar profiles are generated for the SCT 5 terrace at 226 kyrs by subtracting the reacted masses of plagioclase at successive depths from the initial protolith plagioclase concentration.

REFERENCES

Anderson R. S., Densmore A. L. and Ellis M. A. (1999) The generation and degradation of marine terraces. *Basin Res.* **11**, 7–19.

Anima R. J., Ettreim S. L., Edwards B. D. and Stevenson A. J. (2002) Near-shore morphology and late Quaternary geologic framework of the northern Monterey Bay Marine Sanctuary, California. *Mar. Geol.* **181**, 35–54.

Blum A. E. and Stillings L. (1995) Feldspar weathering rates. In *Chemical Weathering Rates of Silicate Minerals* (eds. A. F. White and S. L. Brantley), *Rev. Miner.* **31**, 278–323.

Blum J. D. and Erel Y. (1997) Rb-Sr isotope systematics of a granitic soil chronosequence: the importance of biotite weathering. *Geochim. Cosmochim. Acta* **61**, 3193–3204.

Bluth G. S. and Kump L. R. (1994) Lithologic and climatic controls of river chemistry. *Geochim. Cosmochim. Acta* **58**, 2341–2359.

Bradley W. C. (1957) Origin of marine-terrace deposits in the Santa Cruz Area, California. *Bull. Geol. Soc. Am.* **68**, 421–444.

Bradley W. C. and Griggs G. B. (1976) Form, genesis, and deformation of central California wave-cut platforms. *Geol. Soc. Am. Bull.* **87**, 433–449.

Brantley S. L. (2003) Reaction kinetics of primary rock-forming minerals under ambient conditions. In *Surface and Ground Water, Weathering and Soils: Treatise of Geochemistry*, vol. 5, Elsevier, Amsterdam, pp. 73–118.

Brantley S. L., Chesley J. T. and Stillings L. (1998) Isotopic ratios and release of strontium measured from weathering feldspars. *Geochim. Cosmochim. Acta* **62**, 1493–1500.

Brimhall G. H. and Dietrich W. E. (1987) Constitutive mass balance relations between chemical composition, volume, density, porosity, and strain in metasomatic hydrochemical systems: results on weathering and pedogenesis. *Geochim. Cosmochim. Acta* **51**, 567–587.

Brimhall G. H., Lewis C. J., Ford C., Bratt J., Taylor G. and Warin O. (1991) Quantitative geochemical approach to pedogenesis: importance of parent material reduction, volumetric expansion, and eolian influx in lateralization. *Geoderma* **51**, 51–91.

Buol S. W., Southhard R. J., Gramham R. C. and McDaniel P. A. (2003) *Soil Genesis and Classification*. Iowa State Press, Ames, 539 pp.

Burch T. E., Nagy K. L. and Lasaga A. C. (1993) Free energy dependence of albite dissolution kinetics at 80 °C, and pH 8.8. *Chem. Geol.* **105**, 137–162.

Chadwick O. A., Brimhall G. H. and Hendricks D. M. (1990) From black box to a grey box: a mass balance interpretation of petrogenesis. *Geomorphology* **3**, 369–390.

Clark J. C. (1981) Stratigraphic, paleontology, and geology of the central Santa Cruz Mountains, California Coast Ranges. *U.S. Geol. Survey Prof. Paper* **1168**, 51 pp.

Clayton J. L. (1986) An estimate of plagioclase weathering rate in the Idaho batholith based upon geochemical transport rates. In *Rates of Chemical Weathering of rocks and minerals* (eds. S. M. Coleman and D. P. Dethier). Academic Press, Orlando, pp. 453–466.

Deer W. A., Howie R. A. and Zussman J. (1985) *Rock Forming Minerals: Framework Silicates*. Longman, New York, 672 pp.

Dessert C., Dupre B., Gaillardet J., Francois L. M. and Allegre C. J. (2003) Basalt weathering laws and the impact of basalt weathering on the global carbon cycle. *Chem. Geol.* **202**, 257–273.

Dupre W. R., Chifton H. E. and Hunter R. E. (1980). Modern sedimentary facies of the open Pacific coast and Pleistocene analogs from the Monterey Bay, California. *Quaternary Depositional Environments of the Pacific Coast: Paleogeography Symposium, Pacific Sec.*, pp. 435–453.

Eberl D. D. (2003) User's guide to ROCKJOCK—a program for determining quantitative mineralogy from powder X-ray diffraction data. *U.S. Geol. Survey Open File Rep.* **03–78**.

Eittreim S. L., Anima R. J. and Stevenson A. J. (2002) Seafloor geology of the Monterey Bay area continental shelf. *Mar. Geol.* **181**, 3–34.

El-Sabbagh D. and Garrison R. E. (1990). Silica digenesis in the Santa Cruz Mudstone (Upper Miocene), La Honda Basin, California. In *Geology and Tectonics of the Central California Coast Region, San Francisco to Monterey, Volume and Guidebook* (eds. R. E. Garrison, H. G. Greene, K. R. Hicks, G. E. Weber and T. L. Wright), Pacific Sec. Assoc. Amer. Petrol. Geol., pp. 123–132.

Fleming K., Johnson P. Z. D., Yokoyama Y., Lambeck K. and Chappell J. (1998) Refining the eustatic sea-level curve since the last glacial maximum using far and intermediate field sites. *Earth Planet. Sci. Lett.* **163**, 327–342.

Gislason S. R. and Arnorsson S. (1990) Saturation state of natural waters in Iceland relative to primary and secondary minerals in basalt. In *Fluid–Mineral Interaction: A tribute to H.P. Eugster*, vol. 2 (eds. R. J. Spencer and I. M. Chou), Geochem. Soc., pp. 273–393.

Godderis Y., Francois L. M., Probst A., Schott J., Moncoulon D., Labat D. and Vivolle D. (2006) Modeling weathering processes at the catchment scale: the WITCH numerical model. *Geochim. Cosmochim. Acta* **70**, 1128–1147.

Hanks T. C., Buckman K. R., Lajoie K. R. and Wallace R. E. (1984) Modification of wave-cut and faulting controlled landforms. *J. Geophys. Res.* **89**, 5771–5790.

Harden J. W., Sarna-Wojciki A. M. and Dembroff S. M. (1986) Soils developed on coastal and fluvial terraces near Ventura, California. *U.S. Geol. Survey Bull.* **1590-B**, 34 pp.

Hellmann R. and Tisserand D. (2006) Dissolution kinetics as a function of the Gibbs free energy of reaction: an experimental study based on albite feldspar. *Geochim. Cosmochim. Acta* **70**, 364–383.

Heimsath A. M., Dietrich W. E., Nishiizumi K. and Finkel R. C. (1997) The soil production function and landscape equilibrium. *Nature* **388**, 358–361.

Hobson W. A. and Dahlgren R. A. (1998) A quantitative study of pedrogenesis in California vernal pool wetlands. In *Quantifying Soil Hydromorphology, Soil Sci. Soc. Amer. Spec. Publication*, vol. 54 (eds. M. C. Rabenhorst, J. C. Bell and P. A. McDaniel), Soil Science Soc. Am., St. Louis, pp. 107–127.

Jenny H. (1941) *Factors of Soil Formation*. McGraw-Hill, New York, 385 pp.

Kistler R. W. and Champion D. E. (2001) Rb–Sr whole-rock and mineral ages, K–Ar, $^{40}Ar/^{39}Ar$, U–Pb mineral ages, and strontium, lead, neodymium, and oxygen isotopic compositions for granitic rocks from the Salinian composite terrain, California. *U.S. Geol. Survey Open File Rep.* **01-453**, 1–84.

Lajoie K. R., Ponti D. J., Powell C. L., Mathieson S. A. and Sarna-Wojcicki A. M. (1991) Emergent marine strandlines and associated sediments, coastal California: a record of Quaternary sea-level fluctuations, vertical tectonic movements, climatic changes, and coastal processes. In *Quaternary Nonglacial Geology: Conterminous U.S.*, vol. K-2, pp. 190–213.

Langley-Turnbaugh S. L. and Bockheim J. G. (1998) Mass balance of soil evolution on late Quaternary marine terraces in coastal Oregon. *Geoderma* **84**, 265–288.

Lasaga A. C. (1998) *Kinetic Theory in the Earth Sciences*. Princeton University Press, Princeton, NJ, 528 pp.

Leinen M., Prospero J. M., Arnold E. and Blank M. (1994) Mineralogy of aeolian dust reaching the North Pacific Ocean. 1. Sampling and analysis. *J. Geophys. Res. D* **99**, 21017–21023.

Leo G. W. (1965) The plutonic and metamorphic rocks of teh Ben Lomond Mountain area, Santa Cruz County, California. *Calif. Division of Mines and Geology Special Report* **91**, 27–44.

Lerbeko J. E. (1956) Authigenic montmorillonoid cement in andestic sandstones of Central California. *J. Sediment. Petrol.* **27**, 298–305.

Lichnter P. C., Steefel C. I. and Oelkers E. H. (1996) Reactive transport in porous media. *Rev. Mineral.* **34**, 1–79.

Mahrer K., Steefel C. I., DePaolo D. J. and Viani B. E. (2006) The mineral dissolution rate conundrum: insights from reactive transport modeling of U isotopes and pore fluid chemistry in marine sediments. *Geochim. Cosmochim. Acta* **70**, 337–363.

Merritts D. J., Chadwick O. A., Hendricks D. M., Brimhall G. H. and Lewis C. J. (1992) The mass balance of soil evolution on late Quaternary marine terraces, Northern California. *Geol. Soc. Amer. Bull.* **104**, 1456–1470.

Merritts D. J., Chadwick O. A. and Hendricks D. M. (1991) Rates and processes of soil evolution on uplifted marine terraces, northern California. *Geoderma* **51**, 241–275.

Muhs D. R. (1992) The last interglacial-glacial transition in North America: evidence from uranium-series dating of coastal deposits. In *The Last Interglacial-Glacial Transition in North America, Geological Soc. Amer. Spec. Paper*, vol. 270, pp. 32–51.

Muhs D. R., Simmons K. R., Kennedy G. L. and Rockwell T. K. (2002) The last interglacical period on the Pacific Coast of North America. *GSA Bull.* **114**, 569–592.

Nesbitt H. W. and Young G. M. (1984) Prediction of some weathering trends of plutonic and volcanic rocks based on thermodynamic and kinetic considerations. *Geochim. Cosmochim. Acta* **48**, 1523–1534.

Oelkers E. H. (2001) General kinetic description of multioxide silicate mineral and glass dissolution. *Geochim. Cosmochim. Acta* **65**, 3703–3719.

Oelkers E. H. and Schott J. (1995) Experimental study of anorthite dissolution and the relative mechanism of feldspar hydrolysis. *Geochim. Cosmochim. Acta* **59**, 5039–5053.

Parkhurst D. L. and Appelo C. A. J. (1999) *User's guide to PHREEQC (version 2)—0A Computer Program for the Speciation, Batch Reaction, One Dimensional Transport, and Inverse Geochemical Calculations*. U.S. Geol. Sur. Water Invest. Rep. 99, 219 pp.

Perg L. A., Anderson R. S. and Finkel R. C. (2001) Use of a new ^{10}Be and ^{26}Al inventory method to date marine terraces, Santa Cruz, California, USA. *Geology* **29**, 879–882.

Perg L. A., Anderson R. S. and Finkle R. C. (2003) Use of cosmogenic radionuclides as a sediment tracer in the Santa Cruz littoral cell, California, United States. *Geology* **31**, 299–302.

Riebe C. S., Kirchner J. K. and Finkel R. C. (2003) Long-term rates of chemical weathering and physical erosion from cosmogenic nuclides and geochemical mass balance. *Geochim. Cosmochim. Acta* **67**, 4427–4441.

Riebe C. S., Kirchner J. W., Granger D. E. and Finkel R. C. (2001) Strong tectonic and weak climatic control of long-term chemical weathering rates. *Geology* **29**, 511–514.

Ross D. C. (1972) Petrographic and chemical reconnaissance study of some granitic and gneissic rocks near San Andreas Fault from Bodega Head to Cajon Pass, California. *U.S. Geol. Survey Prof. Paper* **698**, 1–92.

Ruhe R. V. (1956) Geomorphic surfaces and the nature of soils. *Soil Sci.* **82**, 441–445.

Steefel C. I., DePaolo D. J. and Lichtner P. C. (2005) Reactive transport modeling: an essential tool and a new research approach for earth sciences. *Earth Planet. Sci. Lett.* **240**, 539–558.

Stewart B. W., Capo R. C. and Chadwick O. A. (2001) Effects of rainfall on weathering rate, base cation provenance, and Sr isotope composition of Hawaiian soils. *Geochim. Cosmochim. Acta* **65**, 1087–1099.

Stonestrom D. A., White A. F. and Akstin K. C. (1998) Determining rates of chemical weathering in soils–solute transport versus profile evolution. *J. Hydrol.* **209**, 331–345.

Sverdrup K. and Warfvinge P. (1995) Estimating field weathering rates using laboratory kinetics. In *Chemical Weathering Rates of Silicate Minerals*, vol. 31 (eds. A. F. White and S. L. Brantley). Mineral. Soc. Amer., pp. 295–332.

Torrent J. and Nettleton W. D. (1978) Feedback processes in soil genesis. *Geoderma* **20**, 281–287.

Weber, G. E., Simpson, G. Thornberg. J., Nolan, J. M. and Lettis W. R. (1999) Neotectonics and Quaternary geology of the San Gregorio Fault Zone, Santa Cruz and San Mateo Counties, California Geol. Soc. Am. Cordilleran Section Annual Mtg., Guide Book, Berkeley, CA, 83 pp.

White A. F. (2002) Determining mineral weathering rates based on solid and solute weathering gradients: application to biotite weathering in saprolities. *Chem. Geol.* **190**, 69–89.

White A. F. (2003) Natural weathering rates of silicate minerals. In *Surface and Ground Water, Weathering and Soils Treatise of Geochemistry*, vol. 5 (ed. J. I. Drever). Elsevier, Amsterdam, pp. 345–398.

White A. F. and Brantley S. L. (2003) The effect of time on the weathering of silicate minerals: why do weathering rates differ in the laboratory and field? *Chem. Geol.* **202**, 479–506.

White A. F. and Blum A. E. (1995) Effects of climate on chemical weathering rates in watersheds. *Geochim. Cosmochim. Acta* **59**, 1729–1747.

White A. F., Blum A. E., Schulz M. S., Bullen T. D., Harden J. W. and Peterson M. L. (1996) Chemical weathering of a soil chronosequnece on granitic alluvium. 1. Reaction rates based on changes in soil mineralogy. *Geochim. Cosmochim. Acta* **60**, 2533–2550.

White A. F., Blum A. E., Schulz M. S., Vivit D. V., Larsen M. and Murphy S. F. (1998) Chemical weathering in a tropical watershed, Luquillo Mountains, Puerto Rico: I. Long-term versus short-term chemical fluxes. *Geochim. Cosmochim. Acta* **62**, 209–226.

White A. F., Blum A. E., Stonestrom D. A., Bullen T. D., Schulz M. S., Huntington T. G. and Peters N. E. (2001) Differential rates of feldspar weathering in granitic regolths. *Geochim. Cosmochim. Acta* **65**, 847–869.

White A. F., Schulz M. S., Vivi t D. V., Blum A. E., Stonestrom D. A. and Harden J. (2005) Chemical weathering rates of a soil chronosequence on granitic alluvium: III. Hydrochemical evolution and contemporary solute fluxes and rates. *Geochim. Cosmochim. Acta* **69**, 1975–1996.

Zhu C. (2005) In situ feldspar dissolution rates in an aquifer. *Geochim. Cosmochim. Acta* **69**, 1435–1453.

Associate editor: Jacques Schott